Negative refraction of water waves by hyperbolic metamaterials

Leo-Paul Euvé, Kim Pham, Agnès Maurel

Negative refraction of water waves by hyperbolic metamaterials

Leo-Paul Euvé[1], Kim Pham[2], Agnès Maurel[3],†‡

[1]PMMH, ESPCI, Sorbonne Université, Université PSL, 1 rue Jussieu, 75005 Paris, France

[2]IMSIA, CNRS, EDF, CEA, ENSTA Paris, Institut Polytechnique de Paris, 828 Bd des Maréchaux, 91732 Palaiseau, France,

[3]Institut Langevin, ESPCI Paris, PSL University, CNRS, 1 rue Jussieu, 75005 Paris, France,

(Received xx; revised xx; accepted xx)

We study the propagation of water waves in a three-dimensional device alternating open canals and resonant canals with sub-wavelength resonances. The dispersion of water waves in such a medium is obtained by analyzing the full three-dimensional problem and combining Bloch-Floquet analysis with an asymptotic technique. We obtain the closed-forms of the dispersions for resonant canals containing one or two resonators, which depends only on two functions associated with symmetric and antisymmetric modes and on a geometric parameter analogous to the hopping parameter in topological systems. The analysis of the complete band structure reveals frequency ranges alternating between elliptical and hyperbolic dispersions; in particular the hyperbolic regime gives rise to a negative effective water depth with a consequent negative refraction. Throughout the course of our study, our theoretical results are validated by comparison with numerical calculations of the full three-dimensional problem.

Key words: Subwavelength resonators for water waves; elliptic and hyperbolic dispersions; Dirac cone; negative effective water depth; negative refraction; Bloch-Floquet analysis, asymptotic analysis.

1. Introduction

The study of the propagation of water waves in the presence of a periodic distribution of scatterers began with the seminal work of Schnute (1967) on arrays of submerged horizontal circular cylinders, a problem since revisited by Linton (2011). In subsequent studies, other configurations were considered, including periodic variations in bathymetry (Mei 1985; Davies *et al.* 1989; Porter & Porter 2003; Maurel *et al.* 2019), arrays of vertical cylinders extending throughout the fluid depth (Evans & Porter 1999; McIver 2000; Carter 2012) and deformable or elastic floating scatterer arrays (Chou 1998; Meylan *et al.* 2018). In Schnute (1967), Chou (1998), McIver (2000), the Bloch-Floquet formalism was used, allowing the set of scatterers to be identified with a crystal giving rise to Bragg scattering for waves with wavelengths of the same order as the crystal spacing. This

† Email address for correspondence: leo-paul.euve@espci.fr,agnes.maurel@espci.fr
‡ Email address for correspondence: kim.pham@ensta-paris.fr

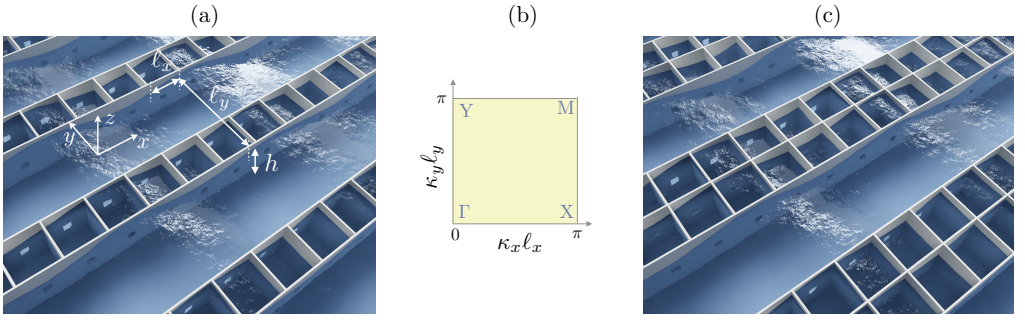

FIGURE 1. Conceptual view of arrays alternating open canals and resonant canals. (a) single-resonant canals contain one resonator along y, (c) doubly-resonant canals contain two resonators along y. (b) shows the irreducible Brillouin zone with $\boldsymbol{\kappa} = (\kappa_x, \kappa_y)$ the Bloch-Floquet wavenumber.

description has been enriched, or at least diversified, thanks to concepts borrowed from condensed matter physics and quantum physics. Dirac cone dispersions have been used to realize zero-refractive-index (ZRI) media for water waves (Wu & Mei 2018) or to produce so-called topologically protected edge modes, in one-dimension (Yang *et al.* 2016; Anglart 2021) and in two-dimensions (Laforge *et al.* 2019; Makwana *et al.* 2020). Anomalous dispersions, such as that reported by Kosaka *et al.* (1998) in a graphene crystal-like photonic crystal, have been used to produce negative refraction of water waves (Farhat *et al.* 2008, 2010; Carter 2012). Recently, an original anomalous dispersion was proposed by Porter (Porter 2021; Porter & Marangos 2022) with inclined plates piercing the surface, thus forcing the energy flow in one direction only. This example is the only one to our knowledge capable of producing negative refraction for water waves in the sub-wavelength regime. In parallel, another strategy has been considered following the work of Veselago (1968) on elliptical dispersion media with two negative effective parameters, gravity and surface depth. However, to date, negative effective gravity in the long wavelength regime has been obtained by Hu *et al.* (2003, 2004) and Huang & Porter (2023) but no device capable of producing negative effective water depth has been proposed.

In the present study, we analyze the dispersion of a periodic medium with subwavelength resonators inspired by the recent works of Euvé and co-workers (Euvé *et al.* 2021*a*,*b*). The medium is composed of alternating open canals and resonant canals formed by one or two resonators, see figure 1. The resonators are cavities whose vertical walls extend through the entire depth of the fluid with completely submerged holes drilled on two opposite walls. We will consider the case where the resonant canal contains a single resonator, called a single-resonant canal (figure 1(a)) and the case where the resonant canal contains two connected resonators, called a doubly-resonant canal (figure 1(c)). Our analysis is based on the Bloch-Floquet formalism combined with asymptotics using an underlying scale separation; this is developed in §2 (the Brillouin zone is shown in figure 1(b) with $\boldsymbol{\kappa} = (\kappa_x, \kappa_y)$ the Bloch-Floquet wavenumber). The derivation of the dispersion relation for a single-resonant canal is performed in §3 and the exercise is repeated more briefly for a doubly-resonant canal in §4. We show that the dispersion relation can be put in the same form in both cases, namely

$$\frac{\kappa_x^2}{\kappa_0^2} + (\chi_s - \chi_a)\sin^2\frac{\kappa_y\ell_y}{2} = \chi_s, \tag{1.1}$$

where χ_s and χ_a are explicit frequency-dependent functions (and they depend on the

number of resonators in the resonant canal) which encapsulate the subwavelength resonances of the symmetric and antisymmetric modes. In particular, we show that the dispersion is governed by a geometrical parameter which is the ratio of the cross-sections of the resonator and the open canal in the unit cell, analogous to the hopping parameter in SSH systems (see *e.g.* Coutant *et al.* (2021)). Finally, in §5, the complete band diagrams of both structures are analyzed revealing transitions from elliptical to hyperbolic dispersions, similar to the topological transitions in the isofrequency surfaces of optical metamaterials alternating subwavelength layers of metal and dielectric Dyachenko *et al.* (2016); in both cases, the anisotropic medium is characterized by an effective water depth tensor. In the hyperbolic regime, one of the water depths is negative and an application to negative refraction is proposed. Throughout the course of our study, the validation of the theoretical results is proposed through the comparison with numerical calculations of the full three-dimensional problem.

2. Preliminaries

We consider an inviscid, incompressible fluid and an irrotational motion. Therefore, the velocity $\boldsymbol{U}(\boldsymbol{r})$ and the velocity potential $\Phi(\boldsymbol{r})$ ($\boldsymbol{r} = (x, y, z)$) are solutions of

$$\operatorname{div} \boldsymbol{U} = 0, \qquad \boldsymbol{U} = \boldsymbol{\nabla}\Phi. \tag{2.1}$$

We consider the harmonic regime with time dependence $e^{-i\omega t}$ (ω is frequency and t is time). The boundary conditions read

$$U_z(x, y, 0) = \frac{\omega^2}{g}\Phi(x, y, 0), \qquad \boldsymbol{U} \cdot \boldsymbol{n} = 0, \text{on the rigid walls}, \tag{2.2}$$

with the origin O at the mean free surface, z directed vertically upwards and where U_z is the vertical component of the velocity, $\boldsymbol{n}$ the normal to the rigid part boundaries and g the gravitional constant.

2.1. *Separation of the scales*

We consider resonant cavities whose vertical walls extend through the entire depth h of the fluid with completely submerged holes drilled on two opposite walls. The dynamics of a resonator are captured through the separation of three scales similar to that used in Euvé *et al.* (2021*a*). The smallest, microscopic scale is associated with the dimensions of the hole, e its width which is also the width of the vertical walls and $\sqrt{s}$ with s its cross section. The intermediate, mesoscopic scale is associated with the dimensions of the three-dimensional (3D) unit cell, ℓ_x, ℓ_y and h. Finally, the largest, macroscopic scale refers to the wavelength $1/k = \sqrt{gh}/\omega$ of the waves that would propagate in the absence of resonators (i.e., at the free surface of the water column of depth h in the shallow water regime). We emphasize that this does not imply that the effective wavenumber κ supported by the metamaterial behaves in the same way, and therefore in (1.1), we do not have necessarily $\sin(\kappa_y \ell_y/2) \simeq (\kappa_y \ell_y)/2$. We also define

$$S_c = \ell_c^2, \quad S = \ell \ell_x, \tag{2.3}$$

the cross sections of the resonant cavity and the open canal with $\ell_c = \ell_x - e$ and
− for the single-resonant canal: , $\ell = \ell_y - \ell_c - 2e$,
− for the doubly-resonant canal: $\ell = \ell_y - 2\ell_c - 3e$.
We thus have

$$\sqrt{s}, e \ll \ell_c, \ell, \ell_x, \ell_y, h \ll 1/k, \tag{2.4}$$

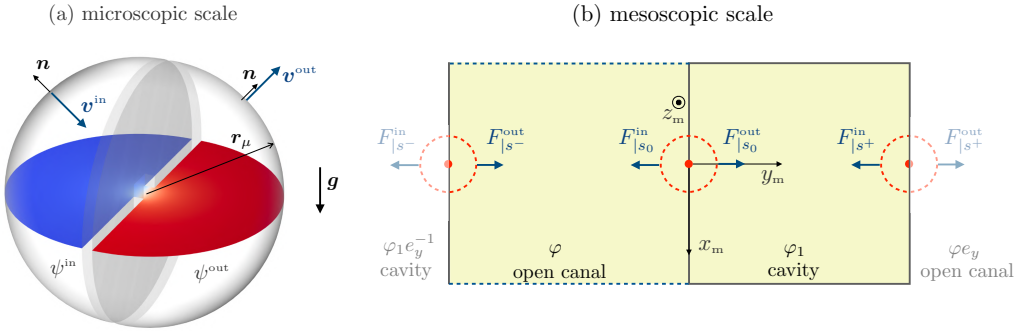

FIGURE 2. (a) Potential flow problem through a pierced wall between two semi-infinite domains (microscopic scale). The horizontal section shows the potential $\psi(\boldsymbol{r}_\mu)$ calculated numerically for a hole with unit section (red and blue indicate the maximum and minimum values of ψ, respectively). (b) Unit cell at the mesoscopic scale for the single-resonant canals. The potentials are constant within each domain (open canal and resonant cavity) and Bloch-Floquet condition applies between adjacent cells.

and, as said before, the wavelength $1/k$ at the largest scale indicates a low frequency regime, not a large effective wavelength $1/\kappa$.

With this separation of scales, the analysis of the problem is similar to that of Marigo *et al.* (2022). It combines an asymptotic homogenization along x and a Bloch-Floquet analysis along y. The homogenization allows to establish the effective propagation equation in the x direction, which provides in part the characteristics of the effective medium. The Bloch-Floquet condition allows to take into account the values of $\kappa_y \in (0, \pi/\ell_y)$ which is necessary to obtain the dispersion relations announced in (1.1). In the following 2.2 and 3.1, we informally present the main steps of the analysis, the more formal derivation of which is given in appendix A.

2.2. *Fluxes and potentials at the microscopic scale*

At the microscopic scale, that is near the opening in the wall, the problem is still that of a potential flow in three-dimension (3D) but the geometry is greatly simplified since the wall has an infinite extension. We consider the problem in a dimensionless form for a hole of unit section in a wall of thickness $e/\sqrt{s}$ separating two unbounded regions Ω^{in} and Ω^{out} (figure 2(a)). Accordingly, we define

$$\boldsymbol{r}_\mu = \frac{\boldsymbol{r}}{\sqrt{s}}, \quad \psi\left(\frac{\boldsymbol{r}}{\sqrt{s}}\right) = \Phi(\boldsymbol{r}), \quad \boldsymbol{v}\left(\frac{\boldsymbol{r}}{\sqrt{s}}\right) = \sqrt{s}\,\boldsymbol{U}(\boldsymbol{r}), \tag{2.5}$$

and the potential ψ and velocity $\boldsymbol{v}$ satisfy

$$\boldsymbol{v} = \boldsymbol{\nabla}_\mu \psi, \quad \operatorname{div}_\mu \boldsymbol{v} = 0, \quad \boldsymbol{v} \underset{r_\mu \to +\infty}{\sim} \begin{cases} -\dfrac{A}{2\pi r_\mu}\,\boldsymbol{n}, & \text{in } \Omega^{\text{in}}, \\ \dfrac{A}{2\pi r_\mu}\,\boldsymbol{n}, & \text{in } \Omega^{\text{out}}, \end{cases} \tag{2.6}$$

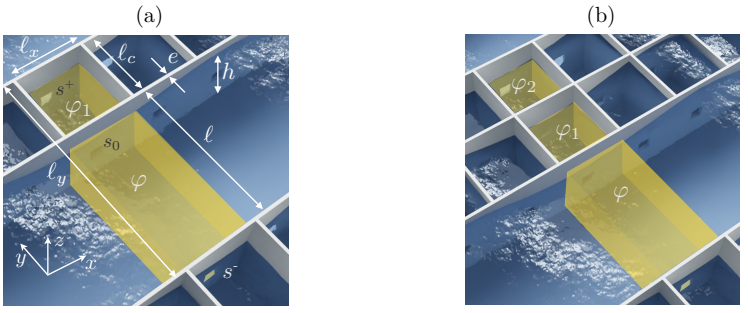

FIGURE 3. Unit cells (highlighted regions) used to derive the effective propagation (a) for the single-resonant canals and (b) for the doubly-resonant canals.

with $\boldsymbol{v}\cdot\boldsymbol{n}=0$ on the the rigid parts and where A is the flux. The solution is written in the form $\psi(\boldsymbol{r}_\mu)=Af(\boldsymbol{r}_\mu)+B$, with A and B two constants and

$$f(\boldsymbol{r}_\mu)\underset{r_\mu\to+\infty}{\sim}\begin{cases}\dfrac{1}{2\pi r_\mu}-\dfrac{b}{2}, & \text{in } \Omega^{\text{in}},\\[2ex] -\dfrac{1}{2\pi r_\mu}+\dfrac{b}{2}, & \text{in } \Omega^{\text{out}},\end{cases} \tag{2.7}$$

where b is a blockage coefficient. We also obtain the form of the constant potentials far from the hole, $\psi^{\text{in}}=-Ab/2+B$ in Ω^{in}, and $\psi^{\text{out}}=Ab/2+B$ in Ω^{out}, and thus

$$A=\frac{1}{b}(\psi^{\text{out}}-\psi^{\text{in}}). \tag{2.8}$$

We now return to our dimensional problem at the mesoscopic scale (figure 2(b)). The fluxes F^{in} and F^{out} are obtained from the previous analysis thanks to the relation $F^{\text{out}}=-F^{\text{in}}=\sqrt{s}A$, which gives

$$F^{\text{out}}=-F^{\text{in}}=\alpha(\varphi^{\text{out}}-\varphi^{\text{in}}),\qquad \alpha=\frac{\sqrt{s}}{b}. \tag{2.9}$$

where φ^{in} (resp. φ^{out}) refer to the value of the potential on the left (resp. on the right) of the drilled hole. For a given shape of the hole, the solution of the potential flow problem, posed on $\psi(\boldsymbol{r}_\mu)$, can be computed numerically by fixing $A=1$ which gives the constant b (see appendix B.1). The value of b depends on $e/\sqrt{s}$ and the shape of the hole cross section. In appendix C, we report the variations of $b(e/\sqrt{s})$ computed for a square-shaped hole.

3. The case of single-resonant canals

In this section we derive the dispersion relation announced in (1.1) along with the closed-form of the functions χ_s and χ_a for the configuration of figure 1(a) alternating open canals and single-resonant canals. The dispersion along the main directions of the Brillouin zone is discussed in relation to the geometrical parameter $\gamma=S_c/S$, the increase of which produces the closure and re-opening of a band-gap along ΓY.

3.1. *Effective propagation*

In the 3D unit cell, sketched in figure 3(a), we introduce the mesoscopic coordinate $\boldsymbol{r}_{\text{m}}=\boldsymbol{r}/h$, $r_{\text{m}}=(x_{\text{m}},y_{\text{m}},z_{\text{m}})$. The result of the asymptotic analysis, whose details are

given in the appendix A, is as follows. The resonant cavity is closed by walls except at the free surface and we have

$$\text{in the cavity}: \quad \Phi(\boldsymbol{r}) = \varphi_1(x), \quad \boldsymbol{U}(\boldsymbol{r}) = \boldsymbol{w}_1(x, \boldsymbol{r}_{\rm m}), \tag{3.1}$$

satisfying

$$\mathrm{div}_{\rm m}\boldsymbol{w}_1 = 0, \qquad \boldsymbol{w}_1(x, x_{\rm m}, y_{\rm m}, 0)\cdot \mathbf{e}_z = \frac{\omega^2}{g}\,\varphi_1(x), \tag{3.2}$$

and $\boldsymbol{w}_1 \cdot \boldsymbol{n} = 0$ on the walls. Next, the region of the open canal is bounded by walls along y only and we have

$$\text{in the open canal}: \quad \Phi(\boldsymbol{r}) = \varphi(x), \quad \boldsymbol{U}(\boldsymbol{r}) = \frac{\partial\varphi}{\partial x}(x)\,\mathbf{e}_x + \boldsymbol{w}(x, \boldsymbol{r}_{\rm m}), \tag{3.3}$$

satisfying

$$\frac{\partial^2\varphi}{\partial x^2} + \mathrm{div}_{\rm m}\boldsymbol{w} = 0, \qquad \boldsymbol{w}(x, x_{\rm m}, y_{\rm m}, 0)\cdot \mathbf{e}_z = \frac{\omega^2}{g}\,\varphi(x), \tag{3.4}$$

$\boldsymbol{w}\cdot\boldsymbol{n} = 0$ on the walls and periodic boundary condition between $x_{\rm m} = \pm\ell_x/2$.
Note that, at the mesoscopic scale, the holes are reduced to points, and at these points, the velocities $(\boldsymbol{w}, \boldsymbol{w}_1)$ have a singularity in $|\boldsymbol{r}_{\rm m}|^{-2}$ which guarantees finite fluxes. These finite fluxes are given by the analysis at the microscopic scale which provided (2.9). Hence, with $F^{\rm in/out}_{|s}(x) = \int_{s^{\rm in/out}} \boldsymbol{w}(x, \boldsymbol{r}_{\rm m})\cdot\mathbf{e}_{\boldsymbol{r}_{\rm m}}\mathrm{d}s$, the fluxes through the surfaces $s^{\rm in/out}$ of the half spheres centred at a singular point with vanishing radius, we obtain

$$F^{\rm out}_{|s}(x) = -F^{\rm in}_{|s}(x) = \alpha(\varphi^{\rm out}_{|s}(x) - \varphi^{\rm in}_{|s}(x)). \tag{3.5}$$

We will now derive the equation governing the effective propagation along x and take into account the Bloch-Floquet condition along y, i.e. when passing from one cell to the others over large distances. To begin with, we integrate the incompressibility relation in (3.2) within a resonant cavity, and we obtain

$$\frac{\omega^2 S_c}{g}\varphi_1 - F^{\rm out}_{|s_0} - F^{\rm in}_{|s^+} = 0, \tag{3.6}$$

with $F^{\rm out}_{|s_0}$ and $F^{\rm in}_{|s^+}$ defined in figure 2(a). Accordingly, we have $\varphi^{\rm in}_{|s_0} = \varphi$, $\varphi^{\rm out}_{|s_0} = \varphi^{\rm in}_{|s^+} = \varphi_1$ and, accounting for the Bloch-Floquet conditions along adjacent cells, $\varphi^{\rm out}_{|s^+} = \varphi e_y$ ($e_y = e^{i\kappa_y\ell_y}$), hence

$$\frac{\omega^2 S_c}{g}\varphi_1 - \alpha(\varphi_1 - \varphi) + \alpha(\varphi e_y - \varphi_1) = 0. \tag{3.7}$$

Next, we integrate the incompressibility relation in (3.4) in the region of the open canal resulting in

$$Sh\frac{\partial^2\varphi}{\partial x^2} + \frac{\omega^2 S}{g}\varphi - F^{\rm out}_{|s^-} - F^{\rm in}_{|s_0} = 0,$$

with $\varphi^{\rm in}_{|s^-} = \varphi_1 e_y^{-1}$, $\varphi^{\rm out}_{|s^-} = \varphi^{\rm in}_{|s_0} = \varphi$ and $\varphi^{\rm out}_{|s_0} = \varphi_1$, and thus the second relation

$$Sh\frac{\partial^2\varphi}{\partial x^2} + \frac{\omega^2 S}{g}\varphi - \alpha(\varphi - \varphi_1 e_y^{-1}) + \alpha(\varphi_1 - \varphi) = 0. \tag{3.8}$$

By defining the quantities

$$\omega_0^2 = \frac{\alpha g}{S_c}, \qquad \kappa_0^2 = \frac{\omega_0^2}{gh}, \qquad \gamma = \frac{S_c}{S}, \tag{3.9}$$

and the non-dimensional frequency $\Omega = \omega/\omega_0$, (3.7) and (3.8) take the following form

$$\begin{cases} (\Omega^2 - 2)\varphi_1 + (1 + e_y)\varphi = 0. \\ \dfrac{1}{\kappa_0^2}\dfrac{\partial^2 \varphi}{\partial x^2} + (\Omega^2 - 2\gamma)\varphi + \gamma(1 + e_y^{-1})\varphi_1 = 0. \end{cases} \tag{3.10}$$

In the limit $\gamma = 0$, we recover the one-dimensional propagation equation for a stratified medium namely: $\partial_{xx}\varphi + (\omega^2/gh)\,\varphi = 0$ as it should be (Porter 2021), see also appendix D.

3.2. *Dispersion and symmetries of the modes*

The dispersion and associated modes are obtained by looking for $\varphi(x) = \varphi e^{i\kappa_x x}$ and $\varphi_1(x) = \varphi_1 e^{i\kappa_x x}$ in (3.10) which takes the form

$$\begin{cases} (\Omega^2 - 2)\varphi_1 + (1 + e_y)\varphi = 0. \\ \gamma(1 + e_y^{-1})\varphi_1 + \left(\Omega^2 - 2\gamma - (\kappa_x/\kappa_0)^2\right)\varphi = 0. \end{cases} \tag{3.11}$$

The solvability condition of (3.11) provides the dispersion relation announced in (1.1) with

$$\chi_s(\Omega) = \Omega^2 - 2\gamma\frac{\Omega^2}{\Omega^2 - 2}, \qquad \chi_a(\Omega) = \Omega^2 - 2\gamma. \tag{3.12}$$

As a result, we obtain the following results along the principal directions of the Brillouin zone :

$$\text{along YM :} \quad \begin{cases} \chi_s = \infty\ (\Omega = \sqrt{2}), & \varphi = 0, & \text{S mode,} \\ \kappa_x = \kappa_0\sqrt{\chi_a}, & \varphi_1 = 0, & \text{A mode,} \end{cases} \tag{3.13}$$

$$\text{along X}\Gamma\text{ :} \qquad \kappa_x = \kappa_0\sqrt{\chi_s}, \qquad \frac{\varphi_1}{\varphi} = -\frac{2}{\Omega^2 - 2}, \qquad \text{S mode,} \tag{3.14}$$

$$\text{along }\Gamma\text{Y :} \qquad \frac{\varphi_1}{\varphi} = -\frac{1 + e_y}{\Omega^2 - 2}, \quad \text{with } \ \gamma(e_y + e_y^{-1}) = \Omega^4 - 2(\gamma + 1)\Omega^2 + 2\gamma, \tag{3.15}$$

(the above dispersion is equivalent to (1.1) along with (3.12) for $\kappa_x = 0$). Note that we call S mode (resp. A mode) a mode which is symmetric (resp. antisymmetric) with respect to the axis $(C, \mathbf{e}_x)$ with C the center of a resonant cavity (that is to say within a shifted unit cell with $y_{\rm m} \in (-\ell_y/2, \ell_y/2)$).

The system (3.11) is degenerate at Y ($\kappa_x = 0$, $e_y = -1$) for $\gamma = 1$ since the discriminant of the system vanishes. From (3.13), this corresponds to the point where the branch of the S mode at $\Omega = \sqrt{2}$ (the pole of χ_s) meets the branch $\kappa_x = \kappa_0\sqrt{\chi_a}$ of the A mode at $\kappa_x = 0$ (with $\chi_a = \Omega^2 - 2$ for $\gamma = 1$). We will see that this corresponds to the appearance of a Dirac point at Y.

To inspect the validity of the obtained dispersion, we consider the following configurations : the resonators have a square cross-section $S_c = \ell_c^2$ with $\ell_c = 5$ cm and wall thickness $e = 0.2$ cm; then, we fix the length of the open canal ℓ to obtain $\gamma = 0.5$, 1 or 2 (hence $\ell \simeq 9.6$, 4.8 or 2.4 cm). The (square) section of the submerged opening is

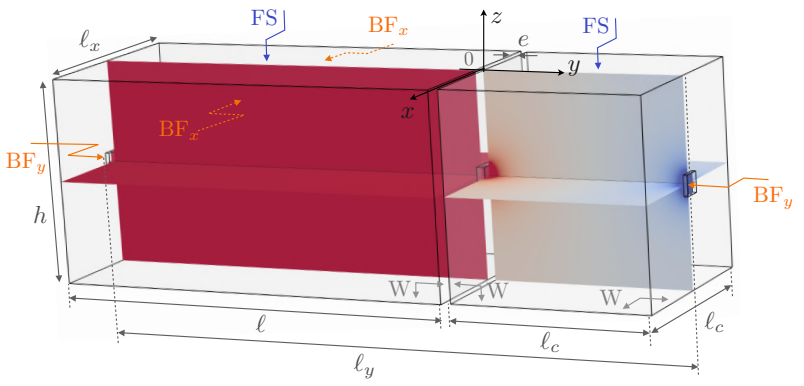

FIGURE 4. Geometry of the three-dimensional unit cell used to compute numerically the dispersion and the Bloch-Floquet modes, and boundary conditions used in the calculations (see main text), with $\ell_y = \ell_c + \ell + 2e$ and $\ell_x = \ell_c + e$.

$s = 0.5 \times 0.5$ cm^2 and the water depth is $h = 5$ cm. The analysis of potential flow through the opening provides the blockage coefficient $b = 1.31$ (see appendix C) and accordingly $\omega_0 = 3.87$ rad.s^{-1}, $\kappa_0 = 5.52$ m^{-1}.

The dispersion in the actual three-dimensional unit cell was calculated numerically. The unit cell is shown in figure 4 for $\ell = 10$ cm. This has been done by using Bloch-Floquet conditions along y (BF$_y$ on faces opposite of the holes at $y = 0$ and $y = -\ell_y$) and along x (on faces opposite $x = \pm\ell_x/2$ and $y \in (-(\ell_c + e), -\ell_y)$), a free water surface condition FS at $z = 0$ (except on regions of the resonator walls piercing the free surface), and rigid wall condition W on the submerged resonator walls and on the sea bottom (see details on the numerics in appendix B.2). In the following, we restrict our representation to ΓY' with Y'($\kappa_y = 0, \kappa_x\ell_y = \pi$) and XM' with M'($\kappa_y\ell_y = \pi, \kappa_x\ell_y = \pi$) since the branches along these directions reaches their asymptotes well before the $\kappa_x\ell_x = \pi$.

The numerical results are presented in figure 5 (grey symbols) together with our theoretical prediction, (1.1) with (3.12) (solid lines). We observe a very good agreement with however a slight loss of accuracy when Ω increases since the assumption of constant potential inside the resonant cavity becomes questionable and at the same time we leave the shallow water regime. Note that an adaptation to greater water depth is possible; this is discussed in Appendix E. Let us now comment on the observed dispersion in the light of the general properties given in (3.13)-(3.15). The two eigenfrequencies at Γ are $\Omega = 0, \sqrt{2(\gamma+1)}$ ($\chi_s = 0$) and the S mode along X'Γ follows the two parts of the branch $\kappa_x = \kappa_0\sqrt{\chi_s}$ corresponding to $\chi_s > 0$. Consequently, a band-gap for $\Omega \in (\sqrt{2}, \sqrt{2(\gamma+1)})$ is observed for any γ. The two eigenfrequencies at Y are $\Omega = \sqrt{2}$ and $\sqrt{2\gamma}$ ($\chi_s = \infty$ for the S mode and $\chi_a = 0$ for the A mode). Along YM, the branch of the S mode stays glued to its asymptote at $\Omega = \sqrt{2}$ and the A mode follows the part of the branch $\kappa_x = \kappa_0\sqrt{\chi_a}$ corresponding to $\chi_a > 0$ ($\Omega > \sqrt{2\gamma}$)†. As expected, the relative positions of the two branches vary depending on whether $\gamma < 1$ or $\gamma > 1$ and they cross for $\gamma = 1$. As a result, the band-gap opened along ΓY for $\gamma < 1$, closes at Y for $\gamma = 1$ with the appearance of a Dirac point, and re-opens for $\gamma > 1$. This behavior is characteristic of topological systems recently studied in the context of water waves (Yang *et al.* 2016;

† For $\gamma < 1$ our model predicts that the two branches along YM' intersect at $\Omega = \sqrt{2}$; in the direct numerics, we observe an avoiding crossing.

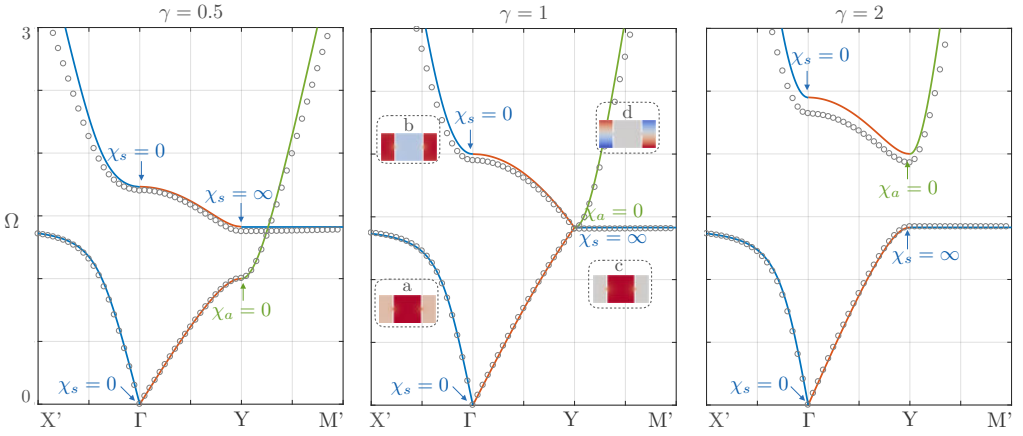

FIGURE 5. Dispersion along the principal directions of the Brillouin zone for the single-resonant canal. The grey symbols are from the direct numerics and the solid lines from (1.1) with (3.12). Along X'Γ, the two branches are associated with S modes; along YM, the blue branch is associated with S modes ($\varphi = 0$), the green branch with A modes ($\varphi_1 = 0$). In (b) the insets shows the patterns in the unit cell centred on the resonator. Because of the degeneracy at Y for $\gamma = 1$, the gap along ΓY at $\gamma = 0.5$ closes at $\gamma = 1$, and reopens at $\gamma = 2$.

Anglart 2021), see also Coutant *et al.* (2021) in one-dimensional and Zheng *et al.* (2019) in two-dimensional acoustic systems.

We conclude this discussion by commenting on the shapes of modes reported in the insets in figure 5(b) for $\gamma = 1$. Along X'Γ, the modes are symmetric; in agreement with (3.14), we observe that φ_1/φ is positive on the first branch (inset a) and it is negative on the second branch (inset b). The first branch then reaches its asymptote at $\Omega = \sqrt{2}$, giving rise to a symmetric mode extended along YM, with $\varphi = 0$ in agreement with (3.13) (inset c). The second branch along YM is associated with antisymmetric modes which is made possible for the single-resonant canal since $\varphi_1 = 0$ in agreement with (3.13) (inset d). The degeneracy at Y is again visible as the shapes of the S and A modes become incompatible at Y.

4. The doubly-resonant canal

We now turn to the configuration in figure 1(c). The unit cell is composed of two identical resonators and a region of the open canal. The second resonator introduces an additional degree of freedom while preserving the form of the dispersion (only χ_s and χ_a will be different) which facilitates the interpretation of the observed phenomena.

4.1. *Analysis of the effective propagation*

We proceed as in the previous section starting with the integration of the incompressibility relation in (3.2) in each resonator which applies for $\Phi(\boldsymbol{r}) = \varphi_1(x)$ and $\Phi(\boldsymbol{r}) = \varphi_2(x)$, see figure 3(b). We obtain

$$\begin{cases} \left(\Omega^2 - 2\right)\varphi_1 + \varphi_2 = -\varphi, \\ \varphi_1 + \left(\Omega^2 - 2\right)\varphi_2 = -e_y\varphi, \end{cases} \tag{4.1}$$

where $e_y = e^{i\kappa_y \ell_y}$ and with now $\ell_y = 2\ell_c + \ell + 3e$. Next, we use (3.4) that we integrate over the region of the open canal within the unit-cell, and we obtain

$$Sh\frac{\partial^2 \varphi}{\partial x^2} + \frac{\omega^2 S}{g}\varphi + \alpha\left(\varphi_1 + \varphi_2 e_y^{-1} - 2\varphi\right) = 0. \tag{4.2}$$

4.2. *Dispersion and symmetries of the modes*

With two resonators, the analysis of the Bloch-Floquet mode symmetry is greatly simplified by introducing the symmetric and antisymmetric parts of the modes in the resonators $\varphi_a = (\varphi_1 + \varphi_2)/2$ and $\varphi_s = (\varphi_1 - \varphi_2)/2$. Next, as before, we look for $\varphi(x) = \varphi e^{i\kappa_x x}$ and $\varphi_{s,a}(x) = \varphi_{s,a} e^{i\kappa_x x}$. By doing so, we obtain from (4.1) and (4.2) the equivalent system

$$\begin{cases} 2\left(\Omega^2 - 1\right)\varphi_s + (1 + e_y)\varphi = 0, \\ 2\left(\Omega^2 - 3\right)\varphi_a + (1 - e_y)\varphi = 0, \\ \gamma(1 + e_y^{-1})\varphi_s + \gamma(1 - e_y^{-1})\varphi_a + \left(\Omega^2 - 2\gamma - (\kappa_x/\kappa_0)^2\right)\varphi = 0, \end{cases} \tag{4.3}$$

whose solvability condition provides the dispersion relation. We recover the form announced in (1.1) with χ_s and χ_a given by

$$\chi_s(\Omega) = \Omega^2 - 2\gamma\frac{\Omega^2}{\Omega^2 - 1}, \qquad \chi_a(\Omega) = \Omega^2 - 2\gamma\frac{\Omega^2 - 2}{\Omega^2 - 3}, \tag{4.4}$$

(instead of (3.12)), with $(\gamma, \kappa_0, \omega_0)$ given in (3.9) and still $\Omega = \omega/\omega_0$. Along the principal directions of the Brillouin zone, we obtain

$$\text{along YM}: \quad \begin{cases} \chi_s = \infty\ (\Omega = 1), & \varphi = \varphi_a = 0, & \text{S mode}, \\ \kappa_x = \kappa_0\sqrt{\chi_a}, & \varphi_s = 0, \quad \dfrac{\varphi_a}{\varphi} = -\dfrac{1}{\Omega^2 - 3}, & \text{A mode}, \end{cases} \tag{4.5}$$

$$\text{along X}\Gamma: \quad \begin{cases} \chi_a = \infty\ (\Omega = \sqrt{3}), & \varphi = \varphi_s = 0, & \text{A mode}, \\ \kappa_x = \kappa_0\sqrt{\chi_s}, & \varphi_a = 0, \quad \dfrac{\varphi_s}{\varphi} = -\dfrac{1}{\Omega^2 - 1}, & \text{S mode}, \end{cases} \tag{4.6}$$

$$\text{along } \Gamma\text{Y}: \quad \frac{\varphi_s}{\varphi} = -\frac{e_y + 1}{2\left(\Omega^2 - 1\right)}, \quad \frac{\varphi_a}{\varphi} = \frac{e_y - 1}{2\left(\Omega^2 - 3\right)}, \\ \text{with} \quad \gamma(e_y + e_y^{-1}) + \Omega^2(\Omega^4 - 4\Omega^2 + 3) - 2\gamma(\Omega^4 - 3\Omega^2 + 1) = 0, \tag{4.7}$$

(the above dispersion relation is equivalent to (1.1) with (4.4), for $\kappa_x = 0$) †. The situation is now the same at Γ and Y. At Γ, the eigenfrequencies correspond to the two zeros of χ_s and the pole of χ_a and at Y, the eigenfrequencies correspond to the two zeros of χ_a and the pole of χ_s.

For $\gamma = 1$, the system (4.3) is degenerate at Y when $\Omega = 1$ and it is degenerate at Γ when $\Omega = \sqrt{3}$ (the discriminant of the system (4.3) vanishes). In the former case at Y, the scenario is the same as for the single-resonant canal; from (4.5), the branch of the S mode at $\Omega = 1$ (the pole of χ_s) meets the branch $\kappa_x = \kappa_0\sqrt{\chi_a}$ of the A mode at $\kappa_x = 0$ (with $\chi_a = (\Omega^2 - 1)(\Omega^2 - 4)/(\Omega^2 - 3)$ for $\gamma = 1$). The situation is the same at Γ for $\Omega = \sqrt{3}$; from (4.6) the branch of the A mode at $\Omega = \sqrt{3}$ (the pole of χ_a) meets the

† Note that the symmetries of the modes correspond to symmetries with respect to $Cx_{\rm m}$ with C the center between the cavities and $y_{\rm m} \in (-\ell_y/2, \ell_y/2)$.

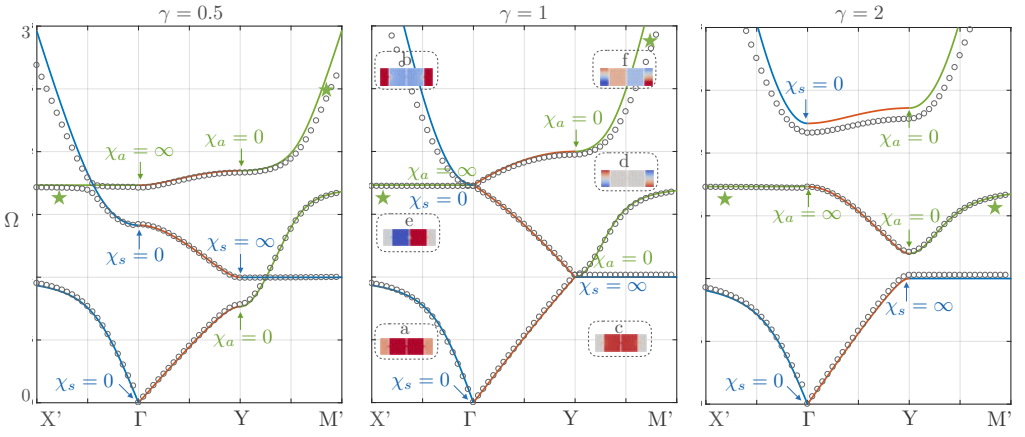

FIGURE 6. Dispersion along the principal directions of the Brillouin zone for the doubly-resonant canal. Same representation as in figure 5. A new branch appears (green stars) associated with the pole of χ_a and one of its two zeros, associated with A modes along X'Γ and YM'. Because of the degeneracies at Γ and Y, the gaps at $\gamma = 0.5$ close at $\gamma = 1$ and re-open at $\gamma = 2$.

branch $\kappa_x = \kappa_0\sqrt{\chi_s}$ of the S mode at $\kappa_x = 0$ (with $\chi_s = \Omega^2(\Omega^2-3)/(\Omega^2-1)$ for $\gamma = 1$). This will lead to the appearance of two Dirac points at Y and at Γ.

We consider the same resonant cavities and open canal, hence again $\gamma = 0.5$, 1 and 2. The holes are the same, so $b = 1.31$, and $\omega_0 = 3.87$ rad.s^{-1}, $\kappa_0 = 5.52$ m^{-1}. Our representation in figure 6 is identical to that in figure 5 (with $\ell_y = 2\ell_c + \ell + 3e$). The dispersion in the three-dimensional unit cell has been calculated numerically (grey symbols) and is compared with the model (1.1) and (4.4) (solid lines). We observe the same very good overall agreement as in figure 5. Among the three branches, two of them were already visible for the single-resonant canals but with the appearance of a new antisymmetric branch (indicated by a star), the branches associated to the S and A modes now behave in the same way. Along XΓ, the two symmetric branches follow the dispersion $\kappa_x = \kappa_0\sqrt{\chi_s}$ with a band-gap when $\Omega \in (1, \sqrt{1+2\gamma})$; the antisymmetric branch is glued to its asymptote at $\Omega = \sqrt{3}$ ($\chi_a = \infty$). Consequently, a Dirac cone appears at Γ where the two branches meet, for $\gamma = 1$, $\Omega = \sqrt{3}$. Along YM', the two antisymmetric branches follow the dispersion $\kappa_x = \kappa_0\sqrt{\chi_a}$ with two band-gaps when $\Omega \in (0, \Omega^-)$ and $\Omega \in (\sqrt{3}, \Omega^+)$ ($\chi_a < 0$, with $\Omega^\pm$ the two zeros of χ_a †) and the symmetric branch is glued to its asymptote at $\Omega = 1$ ($\chi_s = \infty$). With $\Omega^- = 1$ when $\gamma = 1$, the two branches meet when $\Omega = 1$ which gives a Dirac cone at Y.

The shapes of the modes a-d (shown in the insets) on the branches that existed for a single-resonant canal are identical to those reported in figure 5, with $\varphi_a = 0$ for a, b, d and $\varphi_a = \varphi_s = 0$ for c. The new antisymmetric modes, e with $\varphi_s = \varphi = 0$ and f with $\varphi_s = 0$, are made possible by the additional degree of freedom we introduced with the second resonator.

† The two zeros $\Omega^\pm$ of χ_a are the roots of $\Omega^4 - (3+2\gamma)\Omega^2 + 4\gamma = 0$, and whatever the value of γ, $\Omega^- \in (0, \sqrt{2})$ and $\Omega^+ \in (\sqrt{3}, +\infty)$.

5. Elliptic and hyperbolic dispersion, application to negative refraction

In this section, we take the usual representation of effective media in electromagnetism whose simple counterpart for water waves can be deduced from (1.1) when $\kappa_y \ell_y \ll 1$. In this limit, the dispersion relation (1.1) provides in dimensional form

$$h_x \kappa_x^2 + h_y \kappa_y^2 = \frac{\omega^2}{g_e}, \tag{5.1}$$

with

$$h_x = h, \qquad h_y = \frac{(\ell_y \omega_0)^2}{4g}(\chi_s - \chi_a), \qquad g_e = \frac{\Omega^2}{\chi_s}\, g. \tag{5.2}$$

The water depth tensor (with diagonal elements (h_x, h_y)) is equivalent to the permittivity tensor and the effective gravity g_e is equivalent to the effective permeability. With $h_x = h > 0$, the dispersion is elliptical in nature when $h_y > 0$ and $g_e > 0$, and hyperbolic when $h_y < 0$ (the negative index thought by Veselago (1968), with h_x, h_y and g_e negative is not possible). In the limit $\kappa_y \ell_y \ll 1$, we also obtain that the group velocity $\boldsymbol{v}_g = \boldsymbol{\nabla}_{\boldsymbol{\kappa}} \omega$ is

$$\boldsymbol{v}_g \propto h_x \kappa_x \mathbf{e}_x + h_y \kappa_y \mathbf{e}_y, \tag{5.3}$$

and $\boldsymbol{v}_g$ is perpendicular to the isofrequency contour (the curve (κ_x, κ_y) in (5.1) for constant ω value). It is sometimes objected that the directions of the group velocity and the Poynting vector may differ. However, the unambiguous derivation of the expression for the Poynting vector in the equation of energy conservation is made difficult by the fact that (1.1), or (5.1), does not provide an effective model. It is shown in the appendix F that by using a continuity argument with the case of thick plates piercing the free surface, the Poynting vector can be written

$$\boldsymbol{\pi} = 2\omega\xi |\varphi|^2 \left(h_x \kappa_x \mathbf{e}_x + h_y \kappa_y \mathbf{e}_y\right), \tag{5.4}$$

where $\xi = \ell/\ell_y$ is the filling fraction of open canal in the unit cell. Note that when the condition $\kappa_y \ell_y \ll 1$ is not satisfied, (5.1) is still valid using $h_y \to h_y \operatorname{sinc}^2(\kappa_y \ell_y/2)$ and (5.3) is still valid using $h_y \to h_y \operatorname{sinc}(\kappa_y \ell_y)$ (with still $\boldsymbol{v}_g$ perpendicular to the isofrequency contour)†.

5.1. *Band structure and analysis of the isofrequency contours*

We are now interested in the complete band structure in the $(\kappa_x, \kappa_y, \Omega)$ space and in the analysis of the isofrequency contours. We plot in figure 7 the complete band structure obtained from (1.1) using (χ_s, χ_a) in (3.12) for the single-resonant canals and in (4.4) doubly-resonant canals. The colors on the dispersion surface correspond to constant values of $\Omega \in (0, 3)$. We also plot isofrequency contours (white lines) and the dispersion along the principal directions of the Brillouin zone (colored lines as in figures 5 and 6). To interpret the observed isofrequency contours, we start with (5.1) which tells us that the isofrequency contours are elliptical if $(\chi_s - \chi_a) > 0$ ($h_y > 0$) and $\chi_s > 0$ ($g_e > 0$), and they are hyperbolic if $(\chi_s - \chi_a) < 0$ ($h_y < 0$ whatever the sign of g_e). Therefore, in this $\kappa_y \ell_y \ll 1$ approximation, we expect that for a single-resonant canal, with $(\chi_s - \chi_a) = -4\gamma/(\Omega^2 - 2)$, the dispersion is of hyperbolic shape for $\Omega > \sqrt{2}$ and for a doubly-resonant canal, with $(\chi_s - \chi_a) = 4\gamma/((\Omega^2 - 1)(\Omega^2 - 3))$, it is of hyperbolic shape for $\Omega \in (1, \sqrt{3})$, whatever the value of γ. This is roughly consistent with what is observed in figure 7 but must be corrected as $\kappa_y \ell_y$ increases. Indeed, for elliptical and

† We use the function $\operatorname{sinc}(a) = \sin a/a$.

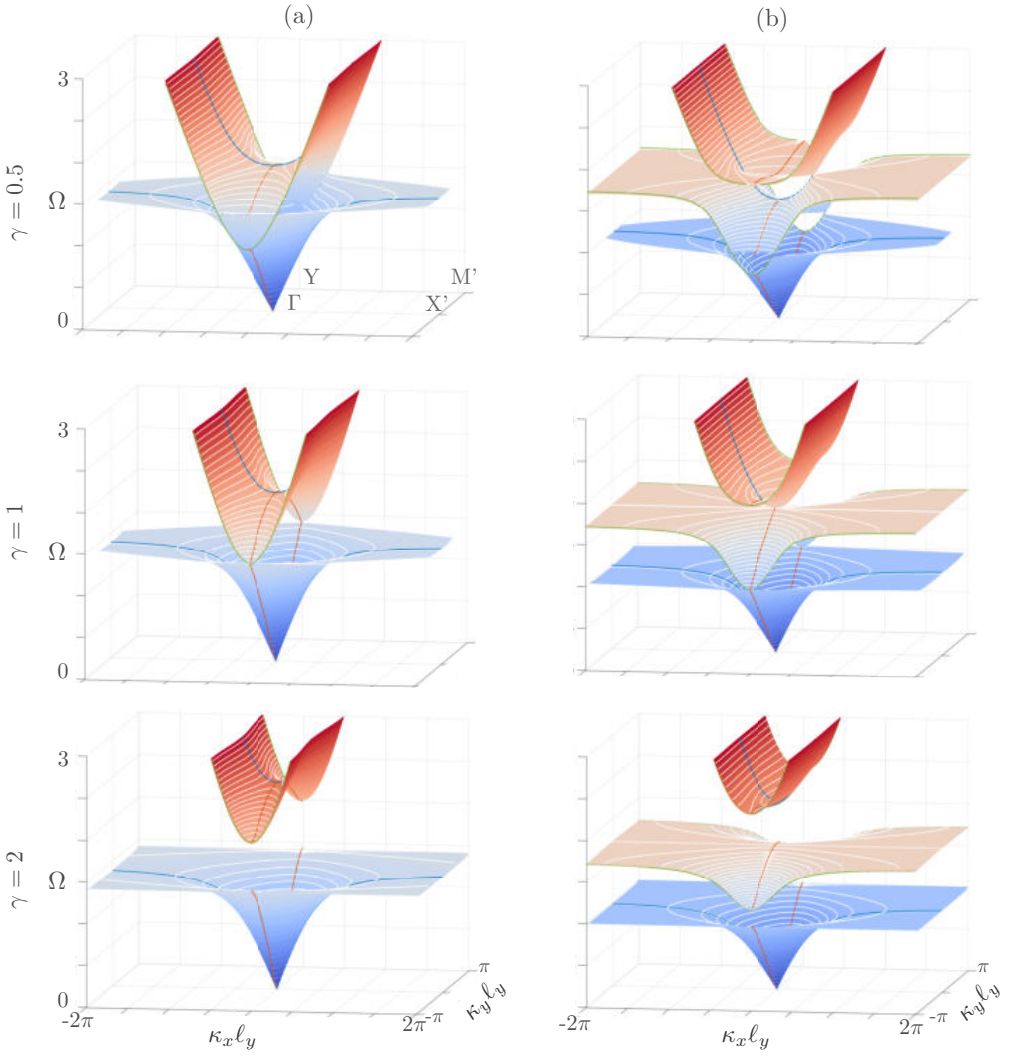

FIGURE 7. Full band structures of a single-resonant (a) and doubly-resonant (b) canal. The white lines show the isofrequency contours and the colored lines show the dispersion in the pass-bands along ΓY (red lines), YM' (blue lines) and XΓ (green lines). As Ω increases, the structures have a dispersion alternating elliptical and hyperbolic isofrequency contours and end up above the last pass-bands of ΓX with a dispersion similar to that of non-resonant closed cavities.

hyperbolic dispersions predicted by (5.1), propagation along ΓY is always possible (there is a solution at $(\kappa_x = 0, \kappa_y \neq 0)$). In fact, the dispersion is elliptical or hyperbolic only in the passbands of ΓY. Outside these regions, ellipses and hyperbolas are deformed by the opening of a gap at $\kappa_x = 0$. This becomes critical for large enough Ω above the last pass-band of ΓY where the dispersion becomes strongly anisotropic. According to (3.12) or (4.4), we then have $\chi_s = \chi_a \simeq \Omega^2$ and thus the isofrequency contours reduce to the two lines $\kappa_x = \pm\omega/\sqrt{gh}$ as in Porter (2021), see also appendix D.

To confirm and complete these theoretical predictions, we performed the following numerical experiments. We solved numerically the full three-dimensional problem with

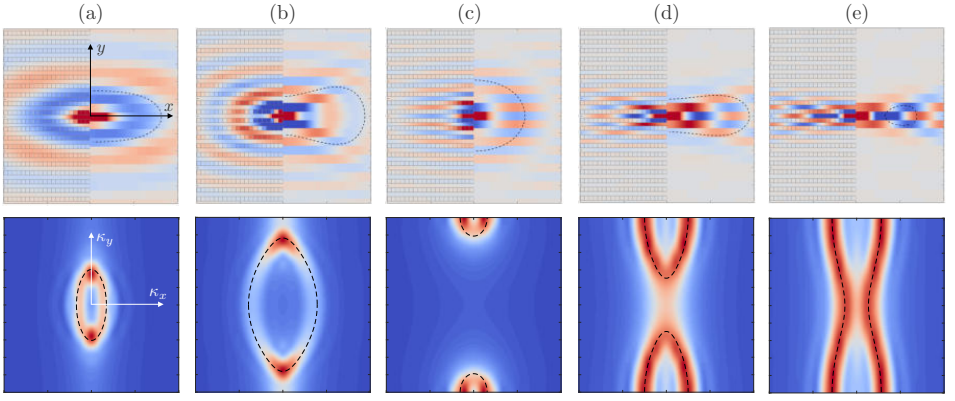

FIGURE 8. Directional emission of a point source through a single-resonant canal (top panels) and corresponding dispersion from the Fourier transform of the fields; the theoretical isofrequency contours, from (1.1) along with (3.12), are shown with dashed black lines (bottom panels). From (a) to (b), $\Omega = 0.62$, 1.12, 1.61, 1.92 and 2.05.

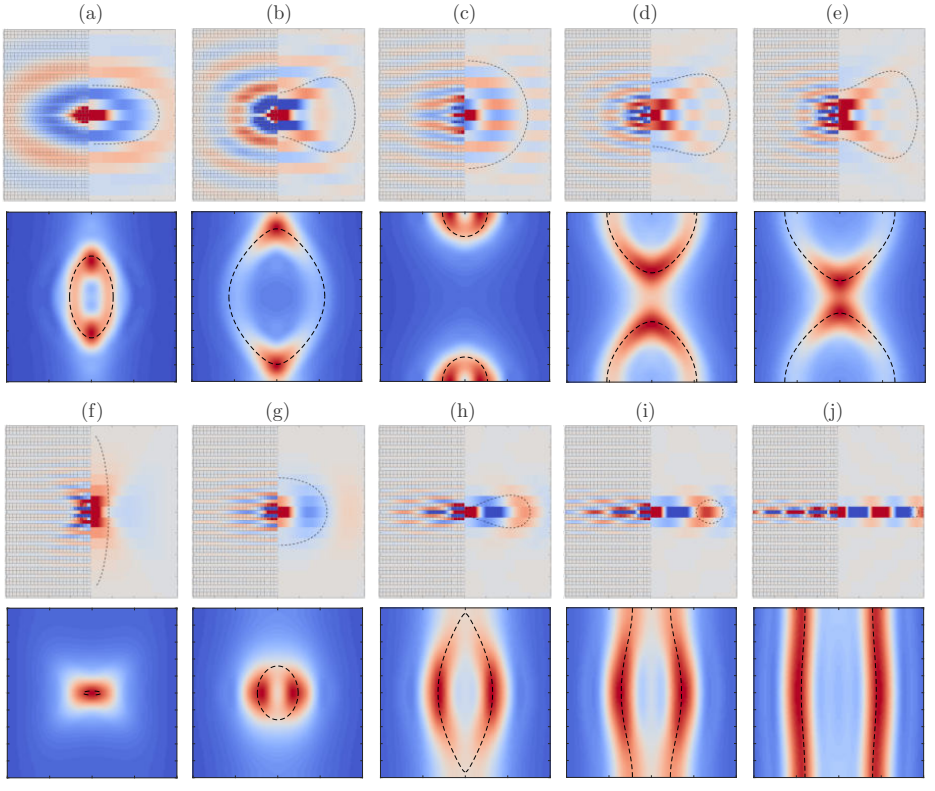

FIGURE 9. Same representation as in figure 8 for doubly-resonant canals (the theoretical isofrequency contours are obtained from (1.1) along with (4.4)). From (a) to (j), $\Omega = 0.50$, 0.80, 1.24, 1.55, 1.61, 1.74, 1.86, 2, 2.05 and 2.24.

a water depth $h = 5$ cm and, in the horizontal plane, a square domain of extension $30\ell_y \times 30\ell_y$. We impose a point excitation at frequency ω at the center of the domain on the free surface corresponding to an open canal (details on the numerics are given in appendix B.3). The results are shown in figures 8 and 9 for the single- and doubly-resonant

canals, respectively (the reported domain is $20\ell_y \times 20\ell_y$). In the figures, the upper panels show the velocity potential fields in the (x, y) plane at the $z = 0$ free surface. We plot for $x < 0$ the raw numerical result (the position of the resonators is visible) and for $x > 0$ we use a trick to reveal the effective propagation on φ by expanding the field in the open canal to the entire unit cell. In these regions, the dashed black line show the extremities of the Poynting vector calculated from (5.4). The lower panels show the Fourier transform of the field in the (κ_x, κ_y) plane as well as the theoretical isofrequency contour at the same frequency (dashed black line).

The results confirm that the isofrequency contours undergo transitions between elliptical and hyperbolic shapes and the agreement between direct numerical and theory is very good. They also confirm the last transition to an ultra-directional emission along x similar to that of closed cavities, and which results from the deformation of hyperbolas for single-resonant canals and from the deformation of ellipses for doubly-resonant canals. We note that propagation in single resonant canals is in general more anisotropic than in doubly- resonant canals. This is particularly visible in the hyperbolic regime with a characteristic X-shaped emission, the X being less open for the upper panels (d-e) in figure 8 than for those in figure 9.

5.2. *Negative refraction produced by hyperbolic dispersion*

Negative refraction, as opposed to positive refraction, refers to a non-classical refraction whose most striking demonstration is made when a beam incident in a regular region is refracted on the same side of the normal to an interface with a metamaterial. To illustrate the ability of our hyperbolic media to produce negative refraction, we performed a numerical experiment in which such an incident beam passes through a slab $x \in (0, L)$ surrounded by regular regions with constant water depth h_0. The slab is composed of simply resonant canals with the same characteristics as in §3 and we used $L = 18\ell_y$ and $h_0 = h$. The incident beam is generated using sources pulsating at the frequency $\Omega = 2$, placed along a segment inclined by an angle $\theta_i = 45°$ with respect to the vertical direction y. In figure 10(a), the incident beam interferes with the waves diffracted by the edges of the segment but the beam emerging at $x = L$ is clearly visible with a well defined angle θ_i and a small aperture. In the region $x > L$, the Fourier transform of the field thus produces a weak extension spot on the dispersion curve centered on $\boldsymbol{k} = k(\cos\theta_i, \sin\theta_i)$ with $k\ell_y = 1.23$, see figure 10(b).

At the chosen frequency, the dispersion in the slab is of hyperbolic type. Since the vertical component of the wavevectors are conserved, $\kappa_y\ell_y = k_y\ell_y = 0.87$, we predict from (1.1) along with (3.12), that $\kappa_x\ell_y = \pm 0.48$. To determine the sign of κ_x, we use the model again and we are now interested in the Poynting vectors. Outside of the slab, $\boldsymbol{\pi}_0$ given by

$$\boldsymbol{\pi}_0 = 2\omega|\varphi|^2\, h_0\, (k_x \mathbf{e}_x + k_y \mathbf{e}_y)\,, \tag{5.5}$$

is simply parallel to $\boldsymbol{k} = (k_x, k_y)$ with $k = \sqrt{k_x^2 + k_y^2}$ satisfying the usual dispersion relation $k \tanh kh_0 = \omega^2/g$. In these regions, $k_x > 0$ hence $\pi_{0x} > 0$, as it should be. In the slab, we rely on the causality principle which imposes that $\pi_x \propto h_x\kappa_x$ in (5.4) must be positive too; with $h_x = h > 0$, we deduce that κ_x is positive hence $\kappa_x\ell_y = 0.48$. It is then sufficient to note that, in the hyperbolic regime, $h_y < 0$ to deduce that $\pi_y \propto h_y\kappa_y < 0$. These predictions are in very good agreement with the results of figure 10. On the one hand, the Fourier transform of the field in $x \in (0, L)$ (figure 10(c)) shows that the wavevector in the slab corresponds to the wave vector $\boldsymbol{\kappa}$ (the white arrow corresponds to the theoretical prediction) with notably $\kappa_x > 0$. On the other hand, the refraction

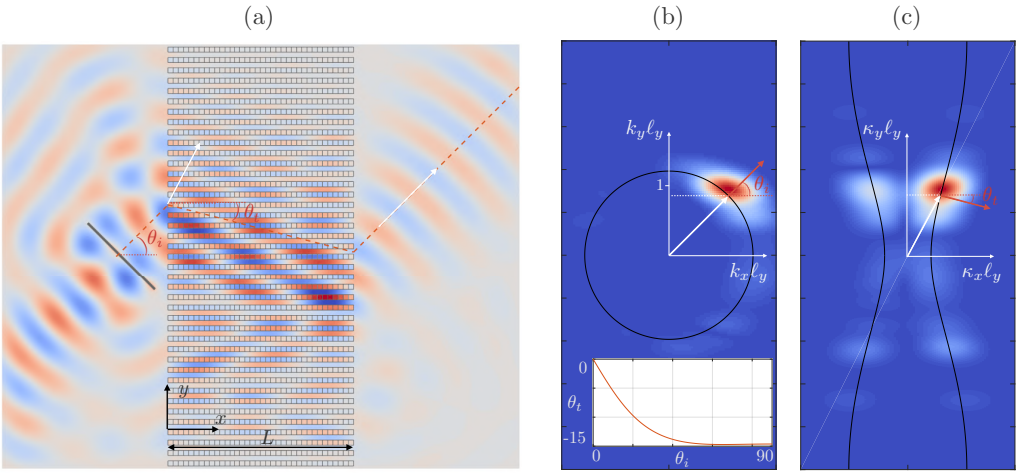

FIGURE 10. (a) Negative refraction in a slab $0 < x < L$ made of resonant canals; the regions $x < 0$ and $x > L$ corresponds to constant water depth regions with water depth $h_0 = h$. The white arrows show the wavevectors inside and outside the slab and the dashed red lines the direction of the Poynting vectors. (b) Wavevectors (white arrows) and Poynting vectors (red arrows) outside and inside the slab.

angle $\theta_t = \text{atan}(\pi_y/\pi_x)$ of the energy flux in the slab, predicted at $\theta_t = -14.2°$ is in agreement with the observed path of the beam refracted in the slab and transmitted at $x = L$ (the theoretical path is indicated in red dotted lines). Let us finally note that the energy of the refracted beam in the slab is particularly directional since for $\theta_i > 40°$ we have $\theta_t \in (14°, 14.7°)$ (inset of figure 10(b)).

6. Conclusion

We have presented a type of subwavelength resonant media capable of producing elliptic or hyperbolic type dispersions for water waves. The dispersion in these media is accurately described by a simple effective model for one or two resonators in the unit cell, in particular the dispersion relation keeps an identical form which naturally encapsulates the symmetry of the Bloch-Floquet modes. Our study has focused on obtaining and validating this dispersion with an application to negative refraction in the hyperbolic regime. We point out that the same mechanism has been recently demonstrated in elastodynamics, with slender beam canals experiencing bending resonances supported by plain elastic canals (Marigo *et al.* 2022). We also note the similarity of the proposed analysis with that conducted in Farhat *et al.* (2008) for an interconnected network of open canals.

To illustrate the validity of the model, we have chosen a rather large hole opening, *i.e.* moderately subwavelength resonances. Choosing a smaller aperture would of course improve the predictivity of the model but would perhaps take us away from realistic practical realizations, due to losses. Moreover, it allowed us to show that the phenomena, predicted in an asymptotic framework that assumes a subwavelength regime, are robust when we push the model towards its limits of validity.

Finally, as mentioned in places in this manuscript, our systems present strong analogies with topological systems recently studied in the context of classical waves. The type of predictive models we have obtained should be useful in extending our study to new

applications. In particular, we have in mind the promising possibility for water waves to travel along interfaces without backscattering regardless the presence of defects or disorder thanks to non-trivial topological phases of which some features, the hopping parameter and topological inversion points associated with degenerate Dirac cones, have already been identified in our model.

Acknowledgment

A.M. and L.-P.E. thank the supports of the Agence Nationale de la Recherche (ANR), under grant 243560 CoProMM.
K.P. thanks the supports of the Agence de l'Innovation de Défense (AID) from the Direction Générale de l'Armement (DGA), under grant 2019 65 0070.

Declaration of interests

The authors report no conflict of interest.

Appendix A. Asymptotic analysis

We will use non-dimensional form of the problem, with $\boldsymbol{r} \to k\boldsymbol{r}$, $\boldsymbol{u} \to \boldsymbol{u}/U_0$ and $\varphi \to k\varphi/U_0$ with $k = \omega/\sqrt{gh}$ and U_0 a characteristic velocity. Accordingly, (2.1)-(2.2) read

$$\text{(a) } \operatorname{div} \boldsymbol{u} = 0, \quad \text{(b) } \boldsymbol{u} = \boldsymbol{\nabla}\varphi, \quad \text{(c) } u_{z|z=0} = \varepsilon\, \varphi_{|z=0}, \tag{A 1}$$

with $\boldsymbol{u} \cdot \boldsymbol{n} = 0$ on the rigid parts and $\varepsilon = \omega\sqrt{h/g} \ll 1$ the small parameter.

A.1. *The mesoscopic scale*

The mesoscopic scale is that of a unit cell $\Omega_t = \Omega_c \cup \Omega$ (Ω_c the region of the cavity and Ω the region of the open canal). Using the rescaled, mesoscopic, coordinate $\boldsymbol{r}_{\rm m} = \boldsymbol{r}/\varepsilon$, with $\boldsymbol{r}_{\rm m} = (x_{\rm m}, y_{\rm m}, z_{\rm m})$, we have

$$\begin{aligned} \Omega &= \{x_{\rm m} \in (-l_x/2, l_x/2), y_{\rm m} \in (-l_y^-, 0), z_{\rm m} \in (-1, 0)\}, \\ \Omega_c &= \{x_{\rm m} \in (-l_x/2, l_x/2), y_{\rm m} \in (0, l_y^+), z_{\rm m} \in (-1, 0)\}. \end{aligned} \tag{A 2}$$

The fields are expanded as follows

$$\varphi = \varphi^0(x, \boldsymbol{r}_{\rm m}) + \varepsilon\varphi^1(x, \boldsymbol{r}_{\rm m}) + \cdots, \quad \boldsymbol{u} = \boldsymbol{u}^0(x, \boldsymbol{r}_{\rm m}) + \varepsilon\boldsymbol{u}^1(x, \boldsymbol{r}_{\rm m}) + \cdots. \tag{A 3}$$

We notice that at the mesoscopic scale, the walls have zero thickness and the holes are reduced to points (finite thickness of the wall and geometry of the hole will be accounted for at the microscopic scale only). In reference to figure 2(a), we call these points P_{s^-}, P_{s_0} and P_{s^+}. Hence the cavity Ω_c is completely closed. The region Ω is bounded by walls at $y_{\rm m} = -l_y^-$ and 0 and we impose periodic boundary conditions

$$\forall\, n \geqslant 0, \quad \varphi^n(x, l_x/2, y_{\rm m}, z_{\rm m}) = \varphi^n(x, -l_x/2, y_{\rm m}, z_{\rm m}), \quad \boldsymbol{r}_{\rm m} \in \Omega, \tag{A 4}$$

(the same for $\boldsymbol{u}^n$). We start with (b) in (A 1) which at the dominant order in ε^{-1} provides $\boldsymbol{\nabla}_{\rm m}\varphi^0 = 0$, hence φ^0 is independent of $\boldsymbol{r}_{\rm m}$ in Ω and in Ω_c. In other words, $\varphi^0(x, y_{\rm m})$ is a function of x only for $y_{\rm m} < 0$ (in Ω) and for $y_{\rm m} > 0$ (in Ω_c). Next, we consider the

problem set on $(\varphi^1, \boldsymbol{u}^0)$. From (a) at the order ε^{-1} and (b-c) at the order ε^0, we obtain

$$\left\{\begin{array}{ll} \mathrm{div}_{\mathrm{m}}\boldsymbol{u}^0 = 0, & \boldsymbol{u}^0 = \boldsymbol{\nabla}_{\mathrm{m}}\varphi^1 + \dfrac{\partial\varphi^0}{\partial x}\,\mathbf{e}_x, \\ u^0_{z|z_{\mathrm{m}}=0} = 0, & \boldsymbol{u}^0\cdot\boldsymbol{n} = 0, \quad \text{on the rigid boundaries,} \end{array}\right. \tag{A 5}$$

which applies in Ω and in Ω_c, and in Ω, the periodic conditions (A 4) apply. Assuming that $\boldsymbol{u}^0$ is regular at $P_{s^\pm}$ and P_{s_0}, the solution to (A 5) reads

$$\boldsymbol{u}^0 = \frac{\partial\varphi^0}{\partial x}\,\mathbf{e}_x, \quad \boldsymbol{r}_{\mathrm{m}} \in \Omega, \qquad \boldsymbol{u}^0 = 0, \quad \boldsymbol{r}_{\mathrm{m}} \in \Omega_c, \tag{A 6}$$

hence $\boldsymbol{u}^0$ is independent of $\boldsymbol{r}_{\mathrm{m}}$ in Ω and in Ω_c. We now use, from (A 1), (a) and (c) at the order ε, namely

$$\mathrm{div}_{\mathrm{m}}\boldsymbol{u}^1 + \frac{\partial u^0_x}{\partial x} = 0, \qquad u^1_{z|z_{\mathrm{m}}=0} = \varphi^0_{|z_{\mathrm{m}}=0}, \tag{A 7}$$

and we integrate the above incompressibility relation over Ω and over Ω_c with $\boldsymbol{u}^0$ in (A 6). We obtain

$$\begin{aligned} 0 &= |\Omega|\,\frac{\partial^2\varphi^0}{\partial x^2}(x, y_{\mathrm{m}} < 0) + \int_{\partial\Omega}\mathrm{div}_{\mathrm{m}}\boldsymbol{u}^1\mathrm{d}\boldsymbol{r}_{\mathrm{m}} \\ &= |\Omega|\,\frac{\partial^2\varphi^0}{\partial x^2}(x, y_{\mathrm{m}} < 0) + S_\Omega\,\varphi^0(x, y_{\mathrm{m}} < 0) + \int_{s^{-,\mathrm{out}}}\boldsymbol{u}^1\cdot\boldsymbol{n}\,\mathrm{d}s_{\mathrm{m}} + \int_{s_0^{\mathrm{in}}}\boldsymbol{u}^1\cdot\boldsymbol{n}\,\mathrm{d}s_{\mathrm{m}}, \quad \text{in } \Omega, \end{aligned} \tag{A 8}$$

with $|\Omega|$ the volume of Ω and S_Ω the surface of Ω at $z_{\mathrm{m}} = 0$, and

$$0 = \int_{\partial\Omega_c}\mathrm{div}_{\mathrm{m}}\boldsymbol{u}^1\mathrm{d}\boldsymbol{r}_{\mathrm{m}} = S_{\Omega_c}\,\varphi^0(x, y_{\mathrm{m}} > 0) + \int_{s_0^{\mathrm{out}}}\boldsymbol{u}^1\cdot\boldsymbol{n}\,\mathrm{d}s_{\mathrm{m}} + \int_{s^{+,\mathrm{in}}}\boldsymbol{u}^1\cdot\boldsymbol{n}\,\mathrm{d}s_{\mathrm{m}}, \quad \text{in } \Omega_c, \tag{A 9}$$

with $|\Omega_c|$ the volume of Ω_c and S_{Ω_c} the surface of Ω_c at $z_{\mathrm{m}} = 0$. The surfaces $s^{-,\mathrm{in/out}}$ are those of half spheres of radius, say $a \to 0$ centred at P_{s^-} (the same for $s^{+,\mathrm{in/out}}$ and $s_0^{\mathrm{in/out}}$). We assume that the fluxes through these surfaces do not vanish that is to say, we assume that $\boldsymbol{u}^1$ is singular at the hole points. The singularity must be of the form

$$\boldsymbol{u}^1(x, \boldsymbol{r}_{\mathrm{m}}) \underset{r_{\mathrm{m}}\to 0}{\sim} \mathrm{sign}(y_{\mathrm{m}})\,\frac{A(x)}{2\pi r_{\mathrm{m}}^2}\,\mathbf{e}_r, \tag{A 10}$$

to ensure the terms of flux in (A 9) and (A 8) to be finite (and the change of sign for $y_{\mathrm{m}} < 0$ and $y_{\mathrm{m}} > 0$ will be justified by the analysis at the microscopic scale).

A.2. *The microscopic scale*

We now move on the microscopic scale in the vicinity of one (generic) hole, and we introduce the rescaled coordinate $\boldsymbol{r}_\mu = \boldsymbol{r}/(\alpha_\mu\varepsilon^3)$, $\boldsymbol{r}_\mu = (x_\mu, y_\mu, z_\mu)$ with

$$\alpha_\mu = \frac{\sqrt{s}}{h\varepsilon^2} = O(1). \tag{A 11}$$

We notice that this choice produces a hole of unitary section at the microscopic scale. At this scale, the sea bottom and the free surface do not exist (they have sent to $\pm\infty$ along x_μ and z_μ) and the problem is reduced to a potential flow problem in an unbounded space, as sketched in figure 2(a). We expand the fields as

$$\varphi = \psi^0(x, \boldsymbol{r}_\mu) + \varepsilon\psi^1(x, \boldsymbol{r}_\mu) + \cdots, \quad \boldsymbol{u} = \varepsilon^{-3}\boldsymbol{v}^{-3}(x, \boldsymbol{r}_\mu) + \varepsilon^{-2}\boldsymbol{v}^{-2}(x, \boldsymbol{r}_\mu) + \cdots. \tag{A 12}$$

The boundary conditions when $r_\mu = |\boldsymbol{r}_\mu| \to +\infty$ are given by matching conditions which tell us that the solution at the microscopic scale when $r_\mu \to +\infty$ has to match the solution at the mesoscopic scale when $r_\mathrm{m} \to 0$, namely

$$\begin{aligned}
&\psi^0(x,\boldsymbol{r}_\mu) + \varepsilon\psi^1(x,\boldsymbol{r}_\mu) + \cdots \underset{r_\mathrm{m}\to 0, r_\mu\to+\infty}{\sim} \varphi^0(x,\boldsymbol{r}_\mathrm{m}) + \varepsilon\varphi^1(x,\boldsymbol{r}_\mathrm{m}) + \cdots\,,\\
&\varepsilon^{-3}\boldsymbol{v}^{-3}(x,\boldsymbol{r}_\mu) + \varepsilon^{-2}\boldsymbol{v}^{-2}(x,\boldsymbol{r}_\mu) + \cdots \underset{r_\mathrm{m}\to 0, r_\mu\to+\infty}{\sim} \boldsymbol{u}^0(x,\boldsymbol{r}_\mathrm{m}) + \varepsilon\boldsymbol{u}^1(x,\boldsymbol{r}_\mathrm{m}) + \cdots\,.
\end{aligned} \tag{A 13}$$

We shall need only the problem set at the dominant order on $(\psi^0, \boldsymbol{v}^{-3})$, which is given, from (A 1), by (a) and (b) at the order ε^{-3}, along with the matching condition on $\boldsymbol{v}^{-3}$ in (A 13) and (A 10), namely

$$\mathrm{div}_\mu \boldsymbol{v}^{-3} = 0, \qquad \boldsymbol{v}^{-3} = \frac{1}{\alpha_\mu}\boldsymbol{\nabla}_\mu\psi^0, \qquad \boldsymbol{v}^{-3}(x,\boldsymbol{r}_\mu) \underset{r_\mu\to+\infty}{\sim} \mathrm{sign}(y_\mu)\,\frac{A(x)}{2\pi\alpha_\mu^2 r_\mu^2}\,\mathbf{e}_{r_\mu}. \tag{A 14}$$

Note that, in (A 14), the behaviour of $\boldsymbol{v}^{-3}$ when $r_\mu \to +\infty$ is consistent with the incompressibility condition, which justifies the choice made in (A 10). We define $f(\boldsymbol{r}_\mu)$ in the relation $\psi^0(x,\boldsymbol{r}_\mu) = A(x)f(\boldsymbol{r}_\mu)/\alpha_\mu + B(x)$ and deduce that

$$f(\boldsymbol{r}_\mu) \underset{r_\mu\to+\infty}{\sim} \frac{1}{2\pi r_\mu} - \frac{b}{2}, \quad y_\mu < 0, \qquad f(\boldsymbol{r}_\mu) \underset{r_\mu\to+\infty}{\sim} -\frac{1}{2\pi r_\mu} + \frac{b}{2}, \quad y_\mu > 0, \tag{A 15}$$

where b is a blockage coefficient, and

$$A(x) = -\alpha_\mu^2 \int_{s^\mathrm{in}} \boldsymbol{v}^{-3}\cdot\mathbf{e}_{r_\mu}\,\mathrm{d}s_{r_\mu} = \alpha_\mu^2 \int_{s^\mathrm{out}} \boldsymbol{v}^{-3}\cdot\mathbf{e}_{r_\mu}\,\mathrm{d}s_{r_\mu} \tag{A 16}$$

is the constant flux. From (A 10), we obtain

$$A(x) = -\int_{s^\mathrm{in}} \boldsymbol{u}^1\cdot\mathbf{e}_{r_\mathrm{m}}\,\mathrm{d}s_\mathrm{m} = \int_{s^\mathrm{out}} \boldsymbol{u}^1\cdot\mathbf{e}_{r_\mathrm{m}}\,\mathrm{d}s_\mathrm{m}. \tag{A 17}$$

We can now come back to (A 8)-(A 9) where we had left the terms of flux. The matching (A 13) at the dominant order on the potentials provides the relations $\varphi^0(x, y_\mathrm{m} < 0) = -A(x)b/(2\alpha_\mu) + B(x)$ and $\varphi^0(x, y_\mathrm{m} > 0) = A(x)b/(2\alpha_\mu) + B(x)$, hence

$$\alpha_\mu\left(\varphi^0(x,y_\mathrm{m}>0) - \varphi^0(x,y_\mathrm{m}<0)\right) = A(x)b, \tag{A 18}$$

(b is known after $f(r_\mu)$ has been calculated numerically). Using further (A 10), we can calculate the fluxes in (A 8)-(A 9).

A.3. *Final expressions*

From what we have seen, we can conclude and establish the relations (3.7) and (3.8). In the main text, we called $\varphi(x) = \varphi^0(x, y_\mathrm{m} < 0)$ and $\varphi_1(x) = \varphi^0(x, y_\mathrm{m} > 0)$ in the unit cell (figure 2(b)). The flux through P_{s_0} corresponds to the integrals over $s^{\mathrm{in/out}} = s_0^{\mathrm{in/out}}$ on the wall at $y_\mathrm{m} = 0$, hence, from (A 17) and (A 18), we have ($\boldsymbol{n} = -\mathbf{e}_{\boldsymbol{r}_\mathrm{m}}$)

$$\int_{s_0^\mathrm{in}} \boldsymbol{u}^1\cdot\boldsymbol{n}\,\mathrm{d}s = -\int_{s_0^\mathrm{out}} \boldsymbol{u}^1\cdot\boldsymbol{n}\,\mathrm{d}s = \frac{\alpha_\mu}{b}\left(\varphi_1 - \varphi\right). \tag{A 19}$$

For the integral over $s^{-,\mathrm{out}}$, (A 17) involves the potential for $y_\mathrm{m} < -l_y^-$, given by the Bloch-Floquet condition (see figure 2(b)) which provides

$$\int_{s^{-\mathrm{out}}} \boldsymbol{u}^1\cdot\boldsymbol{n}\,\mathrm{d}s = \frac{\alpha_\mu}{b}\left(\varphi - \varphi_1 e_y^{-1}\right), \tag{A 20}$$

(with $e_y = e^{i\kappa_y \ell_y}$). Similarly, for the integral over $s^{+,\mathrm{in}}$, (A 17) involves the potential for $y_{\mathrm{m}} > l_y^+$, hence

$$\int_{s^{+,\mathrm{in}}} \boldsymbol{u}^1 \cdot \boldsymbol{n}\, \mathrm{d}s = \frac{\alpha_\mu}{b}\left(\varphi e_y - \varphi_1\right). \tag{A 21}$$

Gathering the above results in (A 8)-(A 9), we obtain

$$\begin{cases} |\Omega|\,\dfrac{\partial^2 \varphi}{\partial x^2} + S_\Omega\,\varphi - \dfrac{\alpha_\mu}{b}\left(\varphi - \varphi_1 e_y^{-1}\right) + \dfrac{\alpha_\mu}{b}\left(\varphi_1 - \varphi\right) = 0, \\ S_{\Omega_c}\,\varphi_1 - \dfrac{\alpha_\mu}{b}\left(\varphi_1 - \varphi\right) + \dfrac{\alpha_\mu}{b}\left(\varphi e_y - \varphi_1\right) = 0, \end{cases} \tag{A 22}$$

which are the dimensionless forms of (3.7) and (3.8) (with $\varepsilon^2 = \omega^2 h/g$, $\alpha_\mu = \sqrt{s}g/(h\omega)^2$, $|\Omega| = S_\Omega = S/h^2$, $S_{\Omega_c} = S_c/h^2$ and remembering that $x \to kx$ with $k^2 = \omega^2/(gh)$).

Appendix B. Details on the numerical calculations

For the numerical resolution of the different problems reported in our study, we used Comsol Multiphysics or the Matlab Partial Differential Equation toolbox. We specify that the choice of the solver is not motivated by the performances/limitations of these numerical tools but rather by the competence of the authors to use one or the other.

B.1. *Resolution of the problem at the microscopic scale*

The problem at the microscopic scale (2.6) has been solved numerically to get the blockage coefficient b in (2.7). This problem is set on $f(\boldsymbol{r}_\mu)$ satisfying the Laplace equation with $\boldsymbol{\nabla} f \cdot \boldsymbol{n} = 0$ on the rigid parts (the vertical wall of thickness $e/\sqrt{s}$ and the walls of the hole) with unitary flux through the whole. We implemented the problem on the geometry shown in figure 11(a) which is composed of:

$$\begin{aligned} &\text{half-hole:} && \left\{x_\mu \in (-1/2, 1/2), y_\mu \in (0, e/(2\sqrt{s})), z_\mu \in (-1/2, 1/2)\right\}, \\ &\text{half-sphere:} && \left\{\left(x_\mu^2 + \left(y_\mu - e/(2\sqrt{s})\right)^2 + z_\mu^2\right) \in (0, R^2)\right\}, \end{aligned} \tag{B 1}$$

with $R \gg e/\sqrt{s}$ in order to recover the limits (2.7) (in practice $R = 10$). The boundary conditions applied to the boundaries of the computational domain are as follows:

$$\begin{aligned} &f = 0, && \text{for } \ x_\mu \in (-1/2, 1/2), y_\mu = 0, z_\mu \in (-1/2, 1/2), \\ &\boldsymbol{\nabla} f \cdot \mathbf{e}_{\boldsymbol{r}_\mu} = \frac{1}{2\pi R^2}, && \text{for } \sqrt{x_\mu^2 + \left(y_\mu - e/(2\sqrt{s})\right)^2 + z_\mu^2} = R,\ y_\mu > e/(2\sqrt{s}. \end{aligned} \tag{B 2}$$

Once f has been computed, we deduce the blockage coefficient

$$b = 2 \lim_{r_\mu \to \infty} \left(f(\boldsymbol{r}_\mu) + \frac{1}{2\pi r_\mu} \right), \tag{B 3}$$

(in practice, for $r_\mu = R$). This problem has been solved using Comsol Multiphysics.

B.2. *Band diagrams*

The band diagram is obtained by solving the three-dimensional direct problem set on $\Phi(\boldsymbol{r})$, (2.1)-(2.2), in the unit cell shown in figure 11(b) (see also 4) with Bloch-Floquet decomposition

$$\Phi(\boldsymbol{r}) = \Phi_{\mathrm{per}}(\boldsymbol{r}) e^{i\boldsymbol{\kappa}\cdot\boldsymbol{r}}, \tag{B 4}$$

where $\Phi_{\mathrm{per}}(\boldsymbol{r})$ is a periodic function with periodicity ℓ_x along x and ℓ_y along y and with $\boldsymbol{\kappa} = \kappa_x \mathbf{e}_x + \kappa_x \mathbf{e}_y$. Numerically, we implemented the weak formulation of the eigenvalue

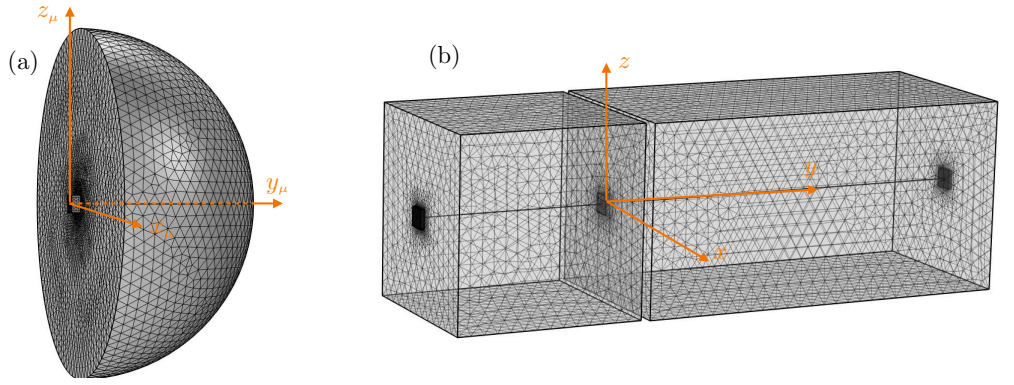

FIGURE 11. (a) Geometry and mesh of the computational domain to solve the microscopic problem on $f(\boldsymbol{r}_\mu)$. (b) Geometry and mesh of the computational domain to solve the eigenvalue problem (B 5) on $\Phi_{\text{per}}(\boldsymbol{r})$ (band diagram).

problem for $\Phi_{\text{per}}(\boldsymbol{r})$ that is to say set on a periodic cell Ω_t. It results that the resolution consists, for a given wavevector $\boldsymbol{\kappa}$, to find the set of $(\omega, \Phi_{\text{per}})$ such that for any (periodic) test function Φ^*_{per} we have

$$\begin{aligned}&\int_{\Omega_t} \left(\nabla\Phi_{\text{per}} \cdot \nabla\Phi^*_{\text{per}} + \kappa^2 \Phi_{\text{per}}\Phi^*_{\text{per}} - i\Phi^*_{\text{per}}\boldsymbol{\kappa} \cdot \nabla\Phi_{\text{per}} + i\Phi_{\text{per}}\boldsymbol{\kappa} \cdot \nabla\Phi^*_{\text{per}}\right) \mathrm{d}\Omega \\ &- \int_{z=0} \frac{\omega^2}{g}\, \Phi_{\text{per}}\Phi^*_{\text{per}} \mathrm{d}S = 0,\end{aligned} \tag{B 5}$$

$\kappa^2 = \boldsymbol{\kappa} \cdot \boldsymbol{\kappa}$. This problem has been solved using Comsol Multiphysics with the weak formulation PDE interface.

B.3. *Numerical experiments with a source term*

For the results reported in figures 8 to 10), the set of equations (2.1)-(2.2) have been modified to account for source terms, specifically

$$\Delta\Phi(\boldsymbol{r}) = S(\boldsymbol{r}). \tag{B 6}$$

We define a elementary source as

$$s_e(\boldsymbol{r}) = e^{-(x^2+y^2+z^2)/d^2}, \qquad d = \ell_x/10. \tag{B 7}$$

The results reported in figures 8 and 9 have been obtained using a point source, and we imposed $S(\boldsymbol{r}) = s_e(\boldsymbol{r})$ with the computational domain being $\{x \in (-15\ell_y, 15\ell_y), y \in (-15\ell_y, 15\ell_y), z \in (-h, 0)\}$.
The results on negative refraction (figure 10) involves an incident beam. In the numerics, we used

$$S(\boldsymbol{r}) = \sum_c s_e(\boldsymbol{r} - \boldsymbol{r}_c) \tag{B 8}$$

with $\boldsymbol{r}_c$ the centers of hundred elementary sources located along a segment inclined of 45° with respect to the $y-$axis (the segment is visible in figure 10).
In both cases, in order to avoid the reflection on the borders of the domain, we used perfectly matched layers (PML) of thickness $2.5\ell_y$. These problems have been solved using the Matlab toolbox Pdetool (partial differential equations using finite element analysis).

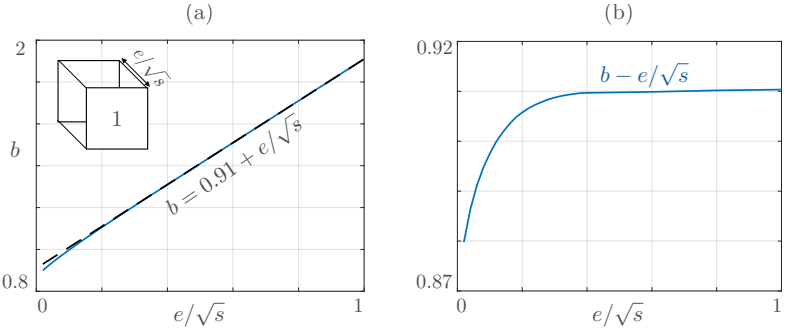

FIGURE 12. (a) Blockage coefficient b of a infinite wall pierced by a square hole with unitary cross-section and normalized length $e/\sqrt{s}$ (solid blue line); a good estimate is given by $b = b_0 + e/\sqrt{s}$, $b_0 = 0.91$, (dashed black line). (b) Variation of $(b - e/\sqrt{s})$ revealing a small shift with respect to the law $b = b_0 + e/\sqrt{s}$ for vanishing e.

Appendix C. Resonance frequency and blockage coefficient

In Euvé *et al.* (2021*a*,*b*) we pointed out the analogy between an underwater resonant cavity for water waves and an acoustic Helmholtz resonator in two-dimensions. Here, the geometry of the cavity is three-dimensional and we will see that, mutatis mutandis, the analogy still holds. The resonance frequency of a Helmholtz resonator, which applies to the acoustic pressure, is obtained by integrating the Helmholtz equation over the cavity and further by assuming that the acoustic velocity in the hole is constant. We repeat this exercise and integrate the incompressibility condition over the cavity with φ_1 the constant potential within the resonator, and $\varphi_{|N}$ the value of the potential at the exit of the neck. Accordingly, we obtain

$$0 = \int \operatorname{div} \boldsymbol{u} \, \mathrm{d}\boldsymbol{r} = \frac{\omega^2 S_c}{g} \varphi_1 + s \, v_{|N}. \tag{C 1}$$

with $v_{|N} = \boldsymbol{u} \cdot \boldsymbol{n}$ at the exit of the resonator neck. Assuming as in the acoustic case that the velocity is constant in the neck of length e, we have $v_{|N} = (\varphi_{|N} - \varphi_1)/e$, hence

$$\left(\omega^2 - \omega_r^2\right) \varphi_1 = -\omega_r^2 \varphi_{|N}, \quad \omega_r^2 = \frac{sg}{eS_c}. \tag{C 2}$$

The above estimate of the resonance frequency does not account for boundary layer effects at the extremities of the hole, due to evanescent fields. This is what has been accounted for in §2.2 where we analyzed the potential flow through a hole, resulting in the resonance frequency ω_0 in (3.9), with $\alpha = \sqrt{s}/b$ in (2.9). The blockage coefficient b, for a hole with unitary cross-section and length $e/\sqrt{s}$, depends only on the shape of the hole cross-section and of $e/\sqrt{s}$. In figure 12 we report the variations of $b(e/\sqrt{s})$ calculated for square shaped hole. Not surprisingly, we obtain $b \simeq b_0 + e/\sqrt{s}$ ($b_0 \simeq 0.91$) and the same result would be obtained for other shapes of hole cross section (with a different value of b_0). Consequently, (3.9), along with (2.9), provides

$$\omega_0^2 = \frac{\alpha g}{S_c} = \frac{sg}{(e + b_0\sqrt{s})S_c}, \tag{C 3}$$

with the hole length e in (C 2) replaced by a so-called effective length $e_{\text{eff}} = e + b_0\sqrt{s}$. We notice in figure 12 that for $e/\sqrt{s} < 1$, the blockage coefficient b_0 varies slightly because the effects of the evanescent fields at each ends of the hole are not independent anymore.

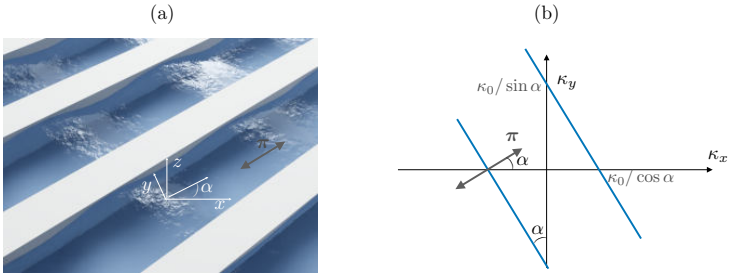

FIGURE 13. (a) The case of arrays of inclined plates studied in (Porter 2021; Porter & Marangos 2022), (b) isofrequency contour at constant ω ($\kappa_0 = \omega/\sqrt{gh}$).

Appendix D. Rigid plates piercing the free surface

We report in this section a quick reminder on the strongly dispersive character of rigid plates piercing the free surface (figure 13(a)), introduced by Porter (Porter 2021; Porter & Marangos 2022) and that we use as a reference case. To begin with, note that, for subwavelength period, this three-dimensional configuration is the exact analogue of the two-dimensional acoustic case, *i.e.* the potential $\varphi(x,y)f(z)$ exactly satisfies the Helmholtz equation

$$(\Delta + k^2)\varphi = 0, \qquad k^2 = \frac{\omega^2}{gh}, \tag{D 1}$$

because no evanescent mode is triggered. For a relative spacing ξ between the plates, the homogenized version of the dispersion is known (Mercier *et al.* 2015; Marigo & Maurel 2017) and takes the following form

$$\operatorname{div} \boldsymbol{w} + \xi \frac{\omega^2}{g}\varphi = 0, \quad \boldsymbol{w} = h\xi\, \mathsf{R}_\alpha \begin{pmatrix} 1 & 0 \\ 0 & 0 \end{pmatrix} \mathsf{R}_\alpha^{-1}\, \boldsymbol{\nabla}\varphi, \tag{D 2}$$

where R_α is the rotation matrix of the angle α. The search for a solution $\varphi(x,y) \propto e^{i(\kappa_y x + \kappa_x y)}$ provides the dispersion

$$\cos\alpha\kappa_x + \sin\alpha\kappa_y = \pm\frac{\omega}{\sqrt{gh}}, \tag{D 3}$$

which gives isofrequency contours composed of two parallel lines (figure 13(a)). Therefore, the water wave energy is forced to follow the direction along the plates, as it should be. As previously said, in the context of our study, the above dispersion for $\alpha = 0$ coincides with (1.1) for $\omega \gg \omega_0$ since from (3.12) and (4.4), $\chi_a \sim \chi_s \sim \Omega^2$, so $\kappa_x = \pm\kappa_0\Omega = \pm\omega/\sqrt{gh}$.

Appendix E. Dependence on the water depth

Here, we consider the possibility of taking into account the finite depth effect $kh \sim 1$. To do so, we define the velocity potential

$$\psi(x,y,z) = \varphi(x,y)f(z), \qquad f(z) = \cosh k(z+h), \tag{E 1}$$

which takes into account the dependence along z of the propagating mode (the wavenumber k now satisfies (**??**)). For single-resonant canals, we proceed as in §3. By integrating the incompressibility condition in the resonant cavity, we obtain

$$\frac{\omega^2 S_c}{g}\,\frac{\cosh kh}{\cosh kh/2}\,\varphi_1 - \alpha(\varphi_1 - \varphi) + \alpha(\varphi e_y - \varphi_1) = 0, \tag{E 2}$$

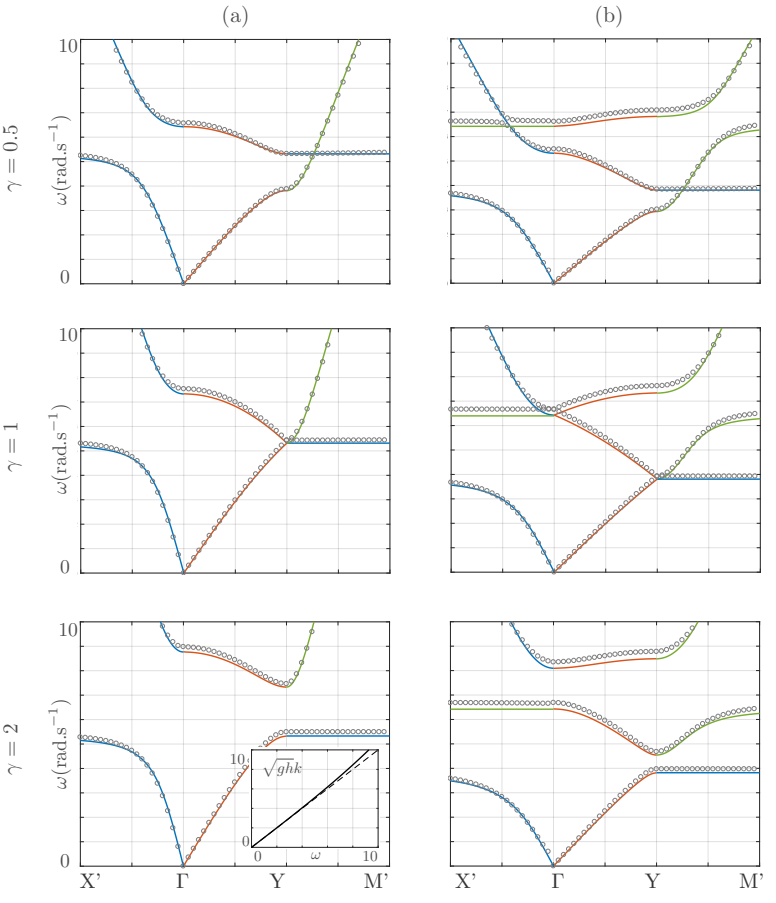

FIGURE 14. Correction of the band diagrams accounting for a dependence of the potential on z, (E 1); (a) for single-resonant canals, to be compared with figure 4 and (b) for doubly-resonant canals, to be compared with figure 6. The inset in (a), $\gamma = 2$, shows the deviation of k satisfying (**??**) with respect the shallow water prediction $k = \omega/\sqrt{gh}$.

(instead of (3.7)). We used the fact that the free surface condition applies to the potential at $z = 0$ and that the fluxes involve the potentials at depth $z^* = -h/2$. Integrating the incompressibility condition in the region of open canal in the unit cell, we obtain in the same way

$$ShF(h)\frac{\partial^2\varphi}{\partial y^2} + \frac{\omega^2 S}{g}\frac{\cosh kh}{\cosh kh/2}\varphi - \alpha(\varphi - \varphi_1 e_y^{-1}) + \alpha(\varphi_1 - \varphi) = 0. \tag{E 3}$$

We used the fact that the integration in the open canal for $z \in (-h, 0)$ makes the integral $\int_{-h}^{0} f(z)\mathrm{d}z$ to appear, and thus

$$F(h) = \frac{\sinh kh}{kh\cosh kh/2}. \tag{E 4}$$

So we obtain the same relations as in (3.10) but with

$$\omega_0^2 = \frac{\alpha g}{S_c}\frac{\cosh kh/2}{\cosh kh}, \qquad \kappa_0^2 = \frac{\omega_0^2}{gh}\frac{kh}{2\sinh kh/2}, \tag{E 5}$$

instead of (3.9). Repeating the exercise for the doubly-resonant canals, we obtain the same relations as in (4.3) with again (E 5) instead of (3.9). We note that ω_0 is now frequency dependent, resulting in a lower resonance frequency; this is consistent to our observations (not reported) when, by increasing h, we leave the shallow water regime. Another consequence is that the interpretation of κ_0 is no longer simple. The results are presented in figure 14; the branches for $\omega > 5$ rad.s^{-1} where the dispersive effects become visible (see inset shows the deviation of k from the shallow water regime $\omega/\sqrt{gh}$) are well corrected when compared to the results in figures 5 and 6. We note, however, that the lower branches are also lightly shifted which gives for $\gamma = 1, 2$ a slightly worth agreement for which we have no explanation.

Appendix F. Poynting vector

The derivation of the Poynting vector that enters the equation of energy balance requires that an effective model be available. The most classical model in the context we are interested in is that of the stratified medium alternating open canals and surfacing piercing plates which as previously said is the exact analog of the acoustic problem. In this context, we have

$$\frac{\xi}{g}\,\ddot{\hat\varphi}(\boldsymbol{x},t) - \operatorname{div}\hat{\boldsymbol{w}}(\boldsymbol{x},t) = 0, \qquad \hat{\boldsymbol{w}}(\boldsymbol{x},t) = \xi h \frac{\partial\hat\varphi}{\partial x}(\boldsymbol{x},t)\mathbf{e}_x, \tag{F 1}$$

so $\hat w_y = 0$ (see *e.g.* Marigo & Maurel (2017) and Zhou Hagström *et al.* (2021)); dot means the time derivative. We multiply the first equation by $\dot{\hat\varphi}$, differentiate the second equation with respect to time and multiply it by $\boldsymbol{\nabla}\dot{\hat\varphi}$, and integrate the sum of the two contributions on a general surface S. We obtain

$$\frac{d}{dt}\int_S \mathcal{E}(\boldsymbol{x},t)\mathrm{d}s + \int_{\partial S}\hat{\boldsymbol{\pi}}(\boldsymbol{x},t)\mathrm{d}l = 0, \tag{F 2}$$

where the first term imples the local energy $\mathcal{E} = \xi(\dot{\hat\varphi})^2/(2g) + \xi h\,(\partial_x\hat\varphi)^2/2$ and the second term is the flux of the Poynting vector through ∂S, with $\hat{\boldsymbol{\pi}}(\boldsymbol{x},t) = -\dot{\hat\varphi}(\boldsymbol{x},t)\hat{\boldsymbol{w}}(\boldsymbol{x},t)$.
In the harmonic regime at the frequency ω, with $\boldsymbol{w}(\boldsymbol{x},\omega') = \boldsymbol{w}(\boldsymbol{x})\delta(\omega-\omega')$, we have

$$\hat{\boldsymbol{w}}(\boldsymbol{x},t) = 2\Re\left(\boldsymbol{w}(\boldsymbol{x})e^{-i\omega t}\right), \quad \dot{\hat\varphi}(\boldsymbol{x},t) = 2\Im\left(\omega\varphi(\boldsymbol{x})e^{-i\omega t}\right).$$

which gives the expression of the Poynting vector averaged in time (on a period $2\pi/\omega$)

$$\boldsymbol{\pi}(\boldsymbol{x}) = 2\omega\Im\left(\varphi^*(\boldsymbol{x})\boldsymbol{w}(\boldsymbol{x})\right). \tag{F 3}$$

Using further that $\boldsymbol{w}(\boldsymbol{x}) = \xi h\partial_x\varphi(\boldsymbol{x})\mathbf{e}_x$ and looking for a solution $\varphi(\boldsymbol{x}) = \varphi e^{i(\kappa_x x+\kappa_y y)}$ we get

$$\boldsymbol{\pi}(\boldsymbol{x}) = 2\omega|\varphi|^2\,\xi h\kappa_x\mathbf{e}_x.$$

As said in the main text, the analysis that provides (1.1) or (5.1) does not provide an effective model as (F 1), mainly because the complexity of the system requires the use of the Bloch-Floquet analysis along y. However we can use the fact that (F 1) is a particular limit of our resonant canal medium (above the resonances) to assume that (5.1) comes from an effective model of the form

$$\frac{\xi}{g_e}\omega^2\varphi(\boldsymbol{x},\omega) + \operatorname{div}\boldsymbol{w}(\boldsymbol{x},\omega) = 0, \qquad \boldsymbol{w}(\boldsymbol{x},\omega) = \xi\begin{pmatrix} h_x & 0\\ 0 & h_y\end{pmatrix}\boldsymbol{\nabla}\varphi(\boldsymbol{x},\omega). \tag{F 4}$$

The form of the system (F 4) provides (1.1) or equivalently (5.1) for a solution $\varphi(\boldsymbol{x}) = \varphi e^{i(\kappa_x x+\kappa_y y)}$ and it allows to recover the limit (F 1) in the time domain where $h_x = h$

and $h_y = 0$ do not depend on ω anymore. If this procedure is legitimate, the balance of energy reads as in (F 2), with a local energy $\mathcal{E}(\boldsymbol{x}, t)$ given by

$$\mathcal{E} = \xi\, \dot{\hat{\varphi}}(\boldsymbol{x}, t) \int_{-\infty}^{\infty} \frac{\ddot{\varphi}(\boldsymbol{x}, \omega)}{g_e(\omega)} e^{-i\omega t} \mathrm{d}\omega + \frac{\hat{\boldsymbol{w}}(\boldsymbol{x}, t)}{\xi} \int_{-\infty}^{\infty} \begin{pmatrix} h_x^{-1}\omega & 0 \\ 0 & h_y^{-1}\omega \end{pmatrix} \dot{\boldsymbol{w}}(\boldsymbol{x}, \omega) e^{-i\omega t} \mathrm{d}\omega,$$

while the expression of the Poynting vector in (F 3) is still valid. With now $\boldsymbol{w}(x)$ given by the second relation in (F 4), and looking as before for a solution $\varphi(\boldsymbol{x}) = \varphi e^{i(\kappa_x x + \kappa_y y)}$ we obtain

$$\boldsymbol{\pi}(\boldsymbol{x}) = 2\omega\xi |\varphi|^2 (h_x \kappa_x + h_y \kappa_y),$$

as announced in (5.4).

REFERENCES

Anglart, A. 2021 Experimental study and modeling of metamaterials for water surface waves. PhD thesis, Université Paris Sciences et Lettres.

Carter, B. 2012 Water-wave propagation through very large floating structures. PhD thesis, Loughborough University.

Chou, T. 1998 Band structure of surface flexural–gravity waves along periodic interfaces. *Journal of Fluid Mechanics* **369**, 333–350.

Coutant, A., Sivadon, A., Zheng, L., Achilleos, V., Richoux, O., Theocharis, G. & Pagneux, V. 2021 Acoustic Su-Schrieffer-Heeger lattice: Direct mapping of acoustic waveguides to the Su-Schrieffer-Heeger model. *Physical Review B* **103** (22), 224309.

Davies, A.G., Guazzelli, E. & Belzons, M. 1989 The propagation of long waves over an undulating bed. *Physics of Fluids A: Fluid Dynamics* **1** (8), 1331–1340.

Dyachenko, P. N., Molesky, S., Petrov, A.Y., Störmer, M., Krekeler, T., Lang, S., Ritter, M., Jacob, Z. & Eich, M. 2016 Controlling thermal emission with refractory epsilon-near-zero metamaterials via topological transitions. *Nature communications* **7** (1), 1–8.

Euvé, L.-P., Pham, K., Petitjeans, P., Pagneux, V. & Maurel, A. 2021*a* Time domain modelling of a Helmholtz resonator analogue for water waves. *Journal of Fluid Mechanics* **920**.

Euvé, L.-P., Piesniewska, N., Maurel, A., Pham, K., Petitjeans, P. & Pagneux, V. 2021*b* Control of the swell by an array of Helmholtz resonators. *Crystals* **11** (5), 520.

Evans, D.V. & Porter, R. 1999 Trapping and near-trapping by arrays of cylinders in waves. *Journal of Engineering Mathematics* **35** (1), 149–179.

Farhat, M., Guenneau, S., Enoch, S. & Movchan, A. 2010 All-angle-negative-refraction and ultra-refraction for liquid surface waves in 2D phononic crystals. *Journal of computational and applied mathematics* **234** (6), 2011–2019.

Farhat, M., Guenneau, S., Enoch, S., Tayeb, G., Movchan, A.B. & Movchan, N.V. 2008 Analytical and numerical analysis of lensing effect for linear surface water waves through a square array of nearly touching rigid square cylinders. *Physical Review E* **77** (4), 046308.

Hu, X., Shen, Y., Liu, X., Fu, R. & Zi, J. 2004 Superlensing effect in liquid surface waves. *Physical Review E* **69** (3), 030201.

Hu, X., Shen, Y., Liu, X., Fu, R., Zi, J., Jiang, X. & Feng, S. 2003 Band structures and band gaps of liquid surface waves propagating through an infinite array of cylinders. *Physical Review E* **68** (3), 037301.

Huang, C. & Porter, R. 2023 Water wave propagation through arrays of closely-spaced surface-piercing vertical barriers .

Kosaka, H., Kawashima, T., Tomita, A., Notomi, M., Tamamura, T., Sato, T. & Kawakami, S. 1998 Superprism phenomena in photonic crystals. *Physical Review B* **58** (16), R10096.

Laforge, N., Laude, V., Chollet, F., Khelif, A., Kadic, M., Guo, Y. & Fleury, R. 2019 Observation of topological gravity-capillary waves in a water wave crystal. *New Journal of Physics* **21** (8), 083031.

Linton, C.M. 2011 Water waves over arrays of horizontal cylinders: band gaps and Bragg resonance. *Journal of Fluid Mechanics* **670**, 504–526.

Makwana, M.P., Laforge, N., Craster, R.V., Dupont, G., Guenneau, S., Laude, V. & Kadic, M. 2020 Experimental observations of topologically guided water waves within non-hexagonal structures. *Applied Physics Letters* **116** (13), 131603.

Marigo, J.-J. & Maurel, A. 2017 Second order homogenization of subwavelength stratified media including finite size effect. *SIAM Journal on Applied Mathematics* **77** (2), 721–743.

Marigo, J.-J., Maurel, A. & Pham, K. 2022 Negative refraction in a single-phase flexural metamaterial with hyperbolic dispersion. *Journal of the Mechanics and Physics of Solids* p. 105126.

Maurel, A., Pham, K. & Marigo, J.-J. 2019 Scattering of gravity waves by a periodically structured ridge of finite extent. *Journal of Fluid Mechanics* **871**, 350–376.

McIver, P. 2000 Water-wave propagation through an infinite array of cylindrical structures. *Journal of Fluid Mechanics* **424**, 101–125.

Mei, C.C. 1985 Resonant reflection of surface water waves by periodic sandbars. *Journal of Fluid Mechanics* **152**, 315–335.

Mercier, J.-F., Cordero, M.-L., Félix, S., Ourir, A. & Maurel, A. 2015 Classical homogenization to analyse the dispersion relations of spoof plasmons with geometrical and compositional effects. *Proceedings of the Royal Society A: Mathematical, Physical and Engineering Sciences* **471** (2182), 20150472.

Meylan, M.H., Bennetts, L.G., Mosig, J.E.M., Rogers, W.E., Doble, M.J. & Peter, M.A. 2018 Dispersion relations, power laws, and energy loss for waves in the marginal ice zone. *Journal of Geophysical Research: Oceans* **123** (5), 3322–3335.

Porter, R. 2021 Plate arrays as a perfectly-transmitting negative-refraction metamaterial. *Wave Motion* **100**, 102673.

Porter, R. & Marangos, C. 2022 Water wave scattering by a structured ridge on the sea bed. *Ocean Engineering* **256**, 111451.

Porter, R. & Porter, D. 2003 Scattered and free waves over periodic beds. *Journal of Fluid Mechanics* **483**, 129–163.

Schnute, J.T. 1967 Scattering of surface waves by submerged circular cylinders. part ii. scattering by an infinite array of cylinders. *Tech. Rep.*. Department of Mathematics, Stanford University.

Veselago, V.G. 1968 Electrodynamics of substances with simultaneously negative electrical and magnetic permeabilities. *Soviet Physics Uspekhi* **10** (4), 504–509.

Wu, S. & Mei, J. 2018 Double Dirac cones and zero-refractive-index media in water waves. *EPL (Europhysics Letters)* **123** (5), 59001.

Yang, Z., Gao, F. & Zhang, B. 2016 Topological water wave states in a one-dimensional structure. *Scientific Reports* **6** (1), 1–6.

Zheng, L.-Y., Achilleos, V., Richoux, O., Theocharis, G. & Pagneux, V. 2019 Observation of edge waves in a two-dimensional Su-Schrieffer-Heeger acoustic network. *Physical Review Applied* **12** (3), 034014.

Zhou Hagström, J., Maurel, A. & Pham, K. 2021 The interplay between Fano and Fabry–Pérot resonances in dual-period metagratings. *Proceedings of the Royal Society A* **477** (2255), 20210632.